This is the Pre-Published Version.

This material may be downloaded for personal use only. Any other use requires prior permission of the American Society of Civil Engineers. This material may be found at https://ascelibrary.org/doi/10.1061/(ASCE)EM.1943-7889.0001623.

The following publication Shi, X. S., Yin, J., & Zhao, J. (2019). Elastic visco-plastic model for binary sand-clay mixtures with applications to one-dimensional finite strain consolidation analysis. Journal of Engineering Mechanics, 145(8), 04019059 is available https://doi.org/10.1061/(ASCE)EM.1943-7889.0001623.

An elastic visco-plastic model for binary sand-clay mixtures with applications to one-dimensional finite strain consolidation analysis

By

Xiusong Shi (Corresponding author)

Department of Civil and Environmental Engineering,

The Hong Kong University of Science and Technology, Hong Kong.

Email: xiusongshi@ust.hk

Jianhua Yin

Department of Civil and Environmental Engineering,

The Hong Kong Polytechnic University, Hung Hom, Kowloon, Hong Kong, China

Tel: (852) 2766-6065, Fax: (852) 2334-6389, Email: cejhyin@polyu.edu.hk

Jidong Zhao

Department of Civil and Environmental Engineering,

The Hong Kong University of Science and Technology, Hong Kong.

Email: jzhao@ust.hk

Nov. 2018

Abstract

The pore water dissipation of sand-clay mixtures is significantly affected by the sand fraction due to nonuniform stress distribution. On the basis of elastic visco-plastic modelling concepts of Yin and Graham (1994), a new elastic visco-plastic (EVP) model based on Lagrangian formulation is proposed to consider the effects of sand fraction in a sand-clay mixture on the time dependent stress-strain behavior at finite strain. In hydraulic dredging and marine deposit improvement projects, the initial water content of mixtures is relatively high, leading to a high compressibility. Therefore, the soil skeleton of the mixtures is fixed to the Lagrangian coordinates to facilitate the definition of soil boundary. The governing equation is formulated by combining an equivalent time concept (Yin and Graham, 1994) with the mixture theory. A finite different method is adopted for the benchmark analysis of boundary-initial value problems. The proposed model contains eight parameters. Seven of them pertain to the clay matrix which can be calibrated from the reference time line, instant time line and consolidation curves of the pure clay in the mixture. The structure parameter represents the inter-granular structure and can be calibrated based on the compressibility of a sand-clay mixture. Two multi-stage oedometer tests (including unloading stages) can be performed to calibrate the model parameters, one on the pure clay and the other one on the sand-clay mixture with a predefined sand fraction. A benchmark analysis of the proposed model reveals a significant difference in excess pore pressure dissipation between Eulerian and Lagrangian coordinates. The calibrated model based on Lagrangian coordinate is found to reproduce the effect of sand fraction on the overall responses of sand-clay mixture well when compared with the experimental data of sand-bentonite mixtures and sand-marine clay mixtures from the literature.

Keywords: Sand fraction effect; Sand-clay mixtures; Equivalent time; Finite difference method; Mixture theory

Introduction

Consolidation of clayey soils with continuous gradations has been extensively investigated in progressive deformation and seepage analysis (Yin and Graham, 1996; Imai *et al.*, 2003; Xie and Leo, 2004; Singh *et al.*, 2014; Zeng *et al.*, 2016). However, natural sedimentary soils are usually gap-graded in terms of particle size distribution due to the presence of certain extent of coarse particles (Satyanaga *et al.*, 2013; Change *et al.*, 2014; Zhou *et al.*, 2016; Ng *et al.*, 2016; Cui *et al*., 2017). Human activities may also lead to gap-graded soils, e.g., in hydraulic dredging engineering (Deng *et al*., 2017), land reclamation projects (Yin, 1999b; Silva, 2016; Shi and Yin, 2018a), debris flow-structure interaction mechanism (Cui *et al*. 2018), and municipal solid waste (MSW) disposal (Marques *et al.*, 2003; Feng *et al.*, 2014; Hubert *et al.*, 2016). Typically, the soils caused by these activities are a mixture of soft matrix with stiff inclusions (e.g., river sand distributed in clay slurry in hydraulic dredging activities; biodegradation-induced matrix mixed with solid materials in MSW). The hydro-mechanical behavior of the mixture depends crucially on two levels of soil structure: the inter-granular structure of the inclusions and the overall structure of the mixture (Graham *et al.*, 1989; Kumar, 1996; Monkul *et al*., 2005; Monkul and Ozden, 2007; Cui *et al*., 2016).

There are two typical hypotheses (termed as Hypothesis A and Hypothesis B) having been proposed in interpreting and modeling the consolidation of clayey soils exhibiting creep (Yin and Feng 2017). In Hypothesis A, a consolidation curve is divided by two separate processes: the primary consolidation coupled with excess pore water pressure dissipation, and the secondary consolidation due to viscous deformation after the end of primary consolidation (Mesri & Castro, 1987; Mesri, 2003). The deformation in primary consolidation can be computed using the classical consolidation theory, e.g., Terzaghi’s theory for small strain (Cui *et al*., 2017a and 2017b) and Gibson’s theory (Gibson *et al.*, 1967) for finite strain consolidation; the viscous deformation can be calculated separately from a secondary compression index (Mesri & Godlewski, 1977; Mesri & Castro, 1987). In Hypothesis B, it is assumed that the viscous deformation of soil skeleton can be induced during and after the primary consolidation process in a coupling process.

The rationality of Hypothesis B approach can be interpreted within the concept of dual-porosity structure of clayey soils. Dejong and Verruijt (1965) classified the soil structure into primary and secondary ones corresponding to primary consolidation and creep deformation, respectively. The secondary structure consists of a cluster of clay particles and micropores between them. The primary structure is composed of clay aggregates (with secondary structure), coarse particles and macropores. In analogy to aggregated soils and fissured porous media (Valliappan & Khalili-Naghadeh, 1990; Borja & Koliji, 2009; Choo & Borja, 2015; Borja & Choo, 2016; Zhao *et al*., 2017), the hydraulic conductivity associated with the primary structure is considered higher than that arising from the secondary structure. For a given surcharge loading, different hydraulic conductivities lead to a gap of excess pore water pressures and subsequent fluids exchange between the micropores and macropores. This indicates that the primary consolidation and creep occur simultaneously.

In Hypothesis A, the model parameters related to the primary consolidation are calibrated based on the total deformation which incorporates the creep deformation. Therefore, it is a phenomenological method, which cannot interpret the real deformation mechanism of soils during the progressive deformation. The model based on Hypothesis A can capture most laboratory oedometer data since the soil sample is very thin, only 20mm, but may not when the soil layer in the field is thick. Time corresponding to ‘end of primary consolidation’ is relatively long in the field analysis (usually several years), and the creep deformation during the primary consolidation cannot be neglected. Therefore, the Hypothesis A-based methods significantly underestimate the settlement of thick soil layers in field analysis (Yin and Feng, 2017), and Hypothesis B has become increasingly popular (Yin and Graham, 1996; Hawlader *et al.*, 2003; Yin and Feng, 2017; Feng and Yin, 2017; Huang *et al*., 2014). In this study, the Hypothesis B approach is adopted for the consolidation analysis of sand-clay mixtures.

In hydraulic dredging and marine deposit improvement projects, the initial water content of the soft soils is relatively high, and a large deformation can be expected (Yin, 1999b; Anderson *et al*., 2001; Hong *et al*., 2010; Zeng *et al*., 2015; Bian *et al.*, 2016 and 2017; Puppala *et al*., 2017). Therefore, classical small strain theory may be questionable. To this end, both small strain and finite strain concept are incorporated in an elastic visco-plastic model to be proposed below, with further assessment and validation of the model performance.

State variables and equivalent time lines

State variables of sand-clay mixtures

A binary sand-clay mixture consisting of soft clay matrix and coarse grain inclusions is considered. The stiffness of the grain inclusions is considered extremely high, such that the overall volume decrease can be regarded solely due to the deformation of the clay matrix during consolidation process. Consequently, the sand volume fraction ϕ_s (defined as the ratio of the volume of sand inclusions to the overall volume of the mixture) decreases with increasing surcharge loading and can be defined as a function of the overall void ratio of mixtures e:

$$\phi_s = \frac{\rho_c - \rho + \rho \upsilon_s}{(1+e)\rho_c} \tag{1}$$

where υ_s is the sand mass fraction, defined as ratio of dry mass of sand inclusions to the overall dry weight of mixtures; ρ is the particle density of mixtures, which can be calculated from the particle densities of the clay matrix ρ_c and the sand inclusions ρ_s:

$$\rho = \frac{\rho_c \rho_s}{\upsilon_s \rho_c + (1-\upsilon_s)\rho_s} \tag{2}$$

The local void ratio of the clay matrix e_c can be expressed as

$$e_c = \frac{e\rho_c}{(1-\upsilon_s)\rho} \tag{3}$$

For a given stress level, if the current strains (local strain of the clay matrix ε_c and overall strain of the mixture ε) are known, the corresponding void ratios can be computed from the strains and the initial void ratios. Logarithmic strains are defined in this study to consider finite deformation of the mixtures. The incremental strains can be defined:

$$\mathrm{d}\varepsilon = -\mathrm{d}\ln(V_t) = -(1-\phi_s)\mathrm{d}\ln(V_c) = (1-\phi_s)\mathrm{d}\varepsilon_c \tag{4}$$

where V_c and V_t are the current volumes of clay matrix and sand-clay mixtures, respectively. The relative difference in stiffness between the clay matrix and coarse inclusions can induce a nonuniform stress in the mixtures (Weng and Tandon, 1988; Tu *et al.*, 2005). Volume-average stress variables are considered in the study, according to the following stress relationship in terms of the overall value and constituent:

$$\sigma' = (1-\phi_s)\sigma'_c + \phi_s\sigma'_s \tag{5}$$

where σ' denotes the overall effective stress of mixtures, σ'_c and σ'_s are the effective stresses of the clay matrix and sand inclusions, respectively. The definition of stress variables is based on a representative volume element (RVE). The RVE contains a statistically representative information of the macrostructure (Zhuang *et al.*, 2014; Zhuang *et al.*, 2015; Quayum *et al.*, 2015). Within this concept, an increase of its volume size should not lead to apparent changes of state variables or governing equations (Hashin, 1983; González & LLorca, 2004; Shi and Herle, 2017). This approach was widely adopted in modelling the behaviour of polymer reinforced composites (He *et al.*, 2016) and multi-phase geo-materials (Zhuang *et al.*, 2017; Shi *et al.*, 2018).

Equivalent time lines of clay matrix

The coarse particles are assumed to be incompressible, thus the hydromechanical behavior of soft clay matrix can be introduced as a reference for evaluating the behavior of the mixtures. The equivalent time concept of the clay matrix would be presented in the sequel of this section. The concept of 'time lines' was proposed by Bjerrum (1967) for interpreting the stress-strain-time relationship of clayey soils. Yin and Graham (1994) provided further mathematical description for the time line concept. They assumed that the deformation was composed of elastic and visco-plastic parts. Following their definitions, the time lines of clay matrix are shown in Fig. 1 in terms of σ'_c-v_c relationship (v_c=e_c +1), including the instant time line, the reference time line, the limit time line and equivalent time lines (dotted lines).

The instant time line describes the instant deformation behavior accompanying with the dissipation of excess pore water pressures. Semi-logarithmic functions between v_c and σ'_c was used in this study. The instant incremental value of v_c is given as

$$\mathrm{d}v_c^e = -\frac{\kappa_c}{\sigma'_c}\mathrm{d}\sigma'_c \tag{6}$$

where κ_c is the slope of the instant time line semi-logarithmic v_c-σ'_c plot. The equivalent time t_e is defined as the time duration for creep from the reference time line to the current state (σ'_c, v_c) at a given stress level (Yin and Graham, 1994). The equivalent time lines in Fig. 1 represent unique v_c-σ'_c relationships for constant values of equivalent time. The reference time line is the equivalent time line at t_e =0. The equivalent time is negative above the reference time line, and becomes positive below the reference time line. The reference time line can be expressed as

$$v_c^{ref} = N_c - \lambda_c \ln\left(\frac{\sigma'_c}{\sigma_r}\right) \tag{7}$$

where N_c and λ_c are model parameters for the reference line of clay matrix, σ_r =1 kPa is a reference stress. Note that N_c and λ_c are affected by the initial water content of clayey soils (e.g., Hong *et al.*, 2010; Shi and Herle, 2015; Horpibulsuk *et al.*, 2016). Hence, the initial water content of the clay matrix in a mixture should be consistent with the pure clay for analysis. A linear creep function is adopted in this work as follows:

$$v_c^{tp} = -\psi_c \ln\left(\frac{t_0 + t_e}{t_0}\right) \tag{8}$$

where t_0 is a curve fitting parameter responsible for the refence time line. Note that the linear creep function gives a satisfactory performance for a time duration of practical interest. However, the creep diminishes with the creep time, and finally reaches the limit time line in Fig. 1. To describe the long-term creep behavior, one can use the nonlinear creep function proposed by Yin (1999a). Within the equivalent time concept, the time dependent deformation behavior follows a relationship between v_c, σ_c', and t_e:

$$v_c = v_c^{ref} + v_c^{tp} = N_c - \lambda_c \ln\left(\frac{\sigma_c'}{\sigma_r}\right) - \psi_c \ln\left(\frac{t_0 + t_e}{t_0}\right) \tag{9}$$

Eq. (9) indicates that the current specific volume of the clay matrix can be approximated by the specific volume at the reference time line under the same effective stress with further creep deformation. The equivalent time can be derived as

$$t_e = t_0 \exp\left(\frac{N_c - v_c}{\psi_c}\right)\left(\frac{\sigma_c'}{\sigma_r}\right)^{-\frac{\lambda_c}{\psi_c}} - t_0 \tag{10}$$

Elastic visco-plastic model

Governing equation within Eulerian coordinate

The increment of specific volume of clay matrix consists of the elastic part $\mathrm{d}v_c^e$ and visco-plastic part $\mathrm{d}v_c^e$. Considering Eqs. (6) and (8), one gets

$$\mathrm{d}v_c = \mathrm{d}v_c^e + \mathrm{d}v_c^{tp} = -\frac{\kappa_c}{\sigma_c'}\mathrm{d}\sigma_c' - \frac{\psi_c}{t_0 + t_e}\mathrm{d}t \tag{11}$$

The elastic part is an instant incremental one associated to the stress level and its increment. Note that Eq. (9) is another interpretation of the current specific volume of the clay matrix. The specific volume on the reference time line can be further decomposed into two parts: the specific volume on the instant time line and a visco-plastic part (a constant value, being expressed as a difference between the instant time line and the reference time line). In this case, the incremental form of Eq. (9) is consistent with Eq. (11).

Typical reference time lines of the clay mixtures in sand-clay mixtures are shown in Fig. 2. The line with a higher sand fraction are located above that with lower sand fraction. This phenomenon is induced by nonuniform stress distribution in the mixtures. An incremental stress ratio μ_σ^c is defined as

$$\mu_\sigma^c = \frac{\mathrm{d}\sigma_c'}{\mathrm{d}\sigma'} \tag{12}$$

Substitution of Eqs (10), (12) into Eq. (11) and applying the effective stress principal to Eq. (11) give

$$\frac{\partial v_c}{\partial t} = -\mu_\sigma^c \frac{\kappa_c}{\sigma_c'}\frac{\partial(\sigma - p)}{\partial t} - \frac{\psi_c}{t_0}\exp\left(\frac{v_c - N_c}{\psi_c}\right)\left(\frac{\sigma_c'}{\sigma_r}\right)^{\frac{\lambda_c}{\psi_c}} \tag{13}$$

Eq. (13) offers a unique relationship between $\partial v_c / \partial t$, σ_c', $\partial \sigma_c / \partial t$ and v_c. The incremental relationship between the specific volume and the strain of the clay matrix can be written as

$$\frac{\partial v_c}{\partial t} = v_c \frac{\partial \ln(v_c)}{\partial t} = -v_c \frac{\partial \varepsilon_c}{\partial t} \tag{14}$$

The volume change due to deformation equals the volume of water out of a soil element. Condition of continuity adopted in classical consolidation theory within Eulerian coordinate is

$$\frac{\partial \varepsilon_c}{\partial t} = -\frac{k_c}{\gamma_w}\frac{\partial^2 p_c}{\partial z^2} \tag{15}$$

where γ_w is the unit weight of water, z is the 1D space variable in Eulerian coordinate, k_c is the hydraulic conductivity of the clay matrix, p_c is the excess pore water pressure in the clay matrix. Considering that the coarse particles impermeable with no water holding capacity (Mitchell, 1993), the overall excess pore water pressure p is the local value p_c. Combining Eqs (13)-15 yields (considering that $\partial\sigma / \partial t$ =0):

$$\frac{k_c}{\gamma_w}\frac{\partial^2 p}{\partial z^2} = \mu_\sigma^c \frac{\kappa_c}{v_c \sigma_c'}\frac{\partial p}{\partial t} - \frac{\psi_c}{v_c t_0}\exp\left(\frac{v_c - N_c}{\psi_c}\right)\left(\frac{\sigma_c'}{\sigma_r}\right)^{\frac{\lambda_c}{\psi_c}} \tag{16}$$

The incremental stress ratio is a state dependent parameter. From the equivalent time lines, one obtains the tangent stiffness of the clay matrix:

$$\frac{\mathrm{d}\sigma_c'}{\mathrm{d}\varepsilon_c} = \frac{v_c \sigma_c'}{\lambda_c} \tag{17}$$

After Shi and Yin (2017), the tangent stiffness of sand-clay mixtures can be approximated by that of the clay mixtures and an additional structure variable:

$$\frac{\mathrm{d}\sigma'}{\sigma_r \mathrm{d}\varepsilon} = \left(\frac{\mathrm{d}\sigma_c'}{\sigma_r \mathrm{d}\varepsilon_c}\right)^{\eta(1-\phi_s)} \tag{18}$$

where η is a structure variable associated with the inter-granular structure, which depends on the sand volume fraction:

$$\eta = \left(\frac{1}{1-\phi_s(1+\tilde{e}_s)}\right)^{\vartheta} \tag{19}$$

where ϑ is a model parameter, $\tilde{e}_s$ is the minimum void ratio of the sand material.

Combining Eqs (4), (12), (17) and (18), the incremental stress ratio is deduced as

$$\mu_\sigma^c = \left(\frac{v_c \sigma_c'}{\lambda_c \sigma_r}\right)^{1-\eta(1-\phi_s)} \tag{20}$$

Substitution of Eq. (20) into (16) gives

$$\frac{k_c}{m_v \gamma_w}\frac{\partial^2 p}{\partial z^2}=\left(\frac{v_c \sigma_c'}{\lambda_c \sigma_r}\right)^{1\text{-}\eta(1-\phi_s)}\frac{\partial p}{\partial t}-\frac{\sigma_c \psi_c}{\kappa_c t_0}\exp\left(\frac{v_c-N_c}{\psi_c}\right)\left(\frac{\sigma_c'}{\sigma_r}\right)^{\frac{\lambda_c}{\psi_c}} \tag{21}$$

where $m_v = \kappa_c/(v_c \sigma_c')$ is the compression coefficient following the instant time line.

Governing equation in Lagrangian coordinates

As stated above, the governing equation formulated within Eulerian coordinates is questionable in case of large strain problems with moving boundaries. In this section, the governing equation will be reformulated within the Lagrangian coordinates.

Considering a soil element in one-dimensional (1D) consolidation, z and ζ are 1D space variables in Eulerian and Lagrangian coordinates, respectively. ζ is independent of the consolidation time, thus the boundary condition can be easily defined. Continuity of solid phase in sand-clay mixtures (consisting of clay and sand particles) in the soil element gives

$$\frac{\partial z}{\partial t}\left[1-(1-\phi_s)n_c\right]=\frac{\partial \zeta}{\partial t}\left[1-(1-\phi_{s0})n_{c0}\right] \tag{22}$$

where n_c is the porosity of the clay matrix, n_{c0} is the corresponding initial value. Considering that $(1-\phi_s)n_c = e/(1+e)$, Eq. (22) can be rearranged as

$$\frac{\partial z}{\partial \zeta}=\frac{1+e}{1+e_0} \tag{23}$$

Condition of continuity for water in the clay matrix (the volume change due to deformation equals the volume of water out of a soil element) gives

$$\frac{\partial}{\partial \zeta}\left[(1-\phi_s)n_c v_{cr}\right]=-\frac{\partial}{\partial t}\left((1-\phi_s)n_c\frac{\partial z}{\partial \zeta}\right) \tag{24}$$

where $v_{cr} = v_f - v_{cs}$ is the relative velocity of fluid in the clay matrix, with v_f denoting the absolute velocity of the fluid, and v_{cs} being the absolute velocity of soil particles in the matrix.

The relative fluid velocity in Eq. (24) is associated with the pore water pressure in the clay matrix using Darcy's law:

$$(1-\phi_s)n_c v_{cr} = -\frac{k_c}{\gamma_w}\frac{\partial p_c}{\partial z} = -\frac{k_c}{\gamma_w}\frac{\partial p}{\partial z} \tag{25}$$

where n_c is the porosity of the clay matrix. Substitution of Eqs (23) and (25) into Eq. (24) yields

$$\frac{(1+e_0)^2}{\gamma_w}\frac{\partial}{\partial \zeta}\left(\frac{k_c}{1+e}\frac{\partial p}{\partial \zeta}\right) = \frac{\partial e}{\partial t} \tag{26}$$

The increment of the overall void ratio is expressed as

$$\frac{\partial e}{\partial t} = -v\frac{\partial \varepsilon}{\partial t} = -v(1-\phi_s)\frac{\partial \varepsilon_c}{\partial t} \tag{27}$$

Combining Eqs (13), (14), (26), and (27), one obtains the governing equation and the overall strain increment for the consolidation analysis (see Appendix-1)

$$\frac{(1+e_0)^2 k_c}{(1+e)^2\gamma_w m_v}\frac{\partial^2(\ln\sigma')}{\partial \zeta^2} = (1-\phi_s)\mu_\sigma^c\frac{\partial(\ln\sigma')}{\partial t} + (1-\phi_s)\frac{\sigma_c'\psi_c}{\sigma'\kappa_c t_0}\exp\left(\frac{v_c-N_c}{\psi_c}\right)\left(\frac{\sigma_c'}{\sigma_r}\right)^{\frac{\lambda_c}{\psi_c}} \tag{28}$$

$$\frac{\partial \varepsilon}{\partial t} = (1-\phi_s)\mu_\sigma^c m_v\frac{\partial \sigma'}{\partial t} + (1-\phi_s)\frac{\psi_c}{v_c t_0}\exp\left(\frac{v_c-N_c}{\psi_c}\right)\left(\frac{\sigma_c'}{\sigma_r}\right)^{\frac{\lambda_c}{\psi_c}} \tag{29}$$

The permeability of the clay matrix is a state variable, which can be approximated by a power law of the local void ratio for the clay matrix according to Mesri and Olson (1971) and widely used by others (Pane and Schiffman, 1997, Dolinar, 2009; Zeng *et al.*, 2011 and 2012):

$$\ln(k_c/k_r) = A_c + \xi_c \ln e_c \tag{30}$$

where k_r =1m/s is a unit reference value, A_c and ξ_c are model parameters, ξ_c is the slope of the permeability curve in double logarithmic relationship, and A_c corresponds to a unit void ratio.

Numerical solution procedure

Initial and boundary conditions

Only initial and boundary conditions within Lagrangian coordinates are discussed. To solve the governing equation in Eq. (28), two kind of boundary conditions are considered: the stress boundary and the seepage boundary. Accordingly, two boundaries, Γ1 for effective stress and Γ2 for stress gradient, are defined. The boundary conditions in Lagrangian coordinates are given as

$$\sigma'(\zeta,t) = \bar{\sigma}(\zeta,t); \zeta \in \Gamma 1, t \in [0,\infty) \tag{31}$$

$$\frac{\partial \sigma'(\zeta,t)}{\partial \zeta} = \bar{q}(\zeta,t); \zeta \in \Gamma 2, t \in [0,\infty) \tag{32}$$

where $\bar{\sigma}'(\zeta,t)$ and $\bar{q}(\zeta,t)$ are the loading stress and prescribed value fluid flow on the boundary, respectively. A uniform initial effective stress of the investigated domain is given as

$$\sigma'(\zeta,0) = \bar{\sigma}_0'(\zeta) \tag{33}$$

Finite difference approach

Combining Eqs (28)-(29) and (31)-(33), the consolidation analysis of sand-clay mixtures can be performed using the finite difference method. The configuration of the finite difference model is shown in Fig. 3. In Lagrangian coordinates, the domain is bounded by the lines ζ =0 and ζ =*h* (*h* is the thickness of soil layer) for 1D consolidation analysis. The domain is further discretized into equal rectangles of size $\delta\zeta$ along ζ axis, with *i* and *j* referring to the ζ (depth) and *t* (time) coordinate, respectively. For point (*i*, *j*) in the grid, the governing equation (28) can be approximated by the following difference equation:

$$\left(\frac{(1+e_0)^2}{2(1+e)^2(1-\phi_s)}c_v\right)_i^j \frac{\tilde{\sigma}_{i+1}^{j+1}+\tilde{\sigma}_{i-1}^{j+1}-2\tilde{\sigma}_i^{j+1}+\tilde{\sigma}_{i+1}^{j}+\tilde{\sigma}_{i-1}^{j}-2\tilde{\sigma}_i^{j}}{(\delta\zeta)^2}=\frac{(\mu_\sigma^c)_i^j}{\delta t}(\tilde{\sigma}_i^{j+1}-\tilde{\sigma}_i^{j})+\left(\frac{\sigma_c'}{\sigma'\kappa_c}w\right)_i^j \quad (33a)$$

$$\tilde{\sigma}=\ln(\sigma')\,;\; c_v=\frac{k_c}{\gamma_w m_v}\,;\; w=\frac{\psi_c}{t_0}\exp\left(\frac{v_c-N_c}{\psi_c}\right)\left(\frac{\sigma_c'}{\sigma_r}\right)^{\frac{\lambda_c}{\psi_c}} \quad (33b)$$

Eq. (33) can be rearranged as

$$f_i^{\,j}\tilde{\sigma}_{i-1}^{j+1}-\left[2f_i^{\,j}+(\mu_\sigma^c)_i^j\right]\tilde{\sigma}_i^{j+1}+f_i^{\,j}\tilde{\sigma}_{i+1}^{j+1}=g_i^j \quad (34a)$$

$$f_i^{\,j}=\left(\frac{(1+e_0)^2}{2(1+e)^2(\delta\zeta)^2(1-\phi_s)}c_v\right)_i^j\delta t \quad (34b)$$

$$g_i^j=-f_i^{\,j}\tilde{\sigma}_{i-1}^{j}-\left[(\mu_\sigma^c)_i^j-2f_i^{\,j}\right]\tilde{\sigma}_i^{j}-f_i^{\,j}\tilde{\sigma}_{i+1}^{j}+\left(\frac{\sigma_c}{\sigma'\kappa_c}w\right)_i^j\delta t \quad (34c)$$

From Eq. (29), the overall strain at the current incremental step can be computed as

$$\varepsilon_i^{j+1}=\varepsilon_i^j+\left[(1-\phi_s)m_v\right]_i^j(\mu_\sigma^c)_i^j(\sigma_i^{j+1}-\sigma_i^j)+\left((1-\phi_s)\frac{w}{v_c}\right)_i^j\delta t \quad (35)$$

Eq. (34a) can be written as the following form:

$$\begin{pmatrix} \alpha_1 & \beta_1 & 0 & 0 & 0 & 0 \\ f_2^{\,j} & -2f_2^{\,j}-(\mu_\sigma^c)_2^j & f_2^{\,j} & 0 & 0 & 0 \\ 0 & f_3^{\,j} & -2f_3^{\,j}-(\mu_\sigma^c)_3^j & f_3^{\,j} & 0 & 0 \\ \cdots & \cdots & \cdots & \cdots & \cdots & \cdots \\ 0 & 0 & 0 & f_{n-1}^{\,j} & -2f_{n-1}^{\,j}-(\mu_\sigma^c)_{n-1}^j & 0 \\ 0 & 0 & 0 & 0 & \alpha_2 & \beta_2 \end{pmatrix}\begin{pmatrix}\tilde{\sigma}_1^{j+1} \\ \tilde{\sigma}_2^{j+1} \\ \tilde{\sigma}_3^{j+1} \\ \cdots \\ \tilde{\sigma}_{n-1}^{j+1} \\ \tilde{\sigma}_n^{j+1}\end{pmatrix}=\begin{pmatrix} g_1^j \\ g_2^j \\ g_3^j \\ \cdots \\ g_{n-1}^j \\ g_n^j\end{pmatrix} \quad (36)$$

The boundary conditions can be described by choosing suitable values of $\alpha_1, \beta_1, \alpha_2$, and β_2. If the top (bottom) boundary is freely draining, $\alpha_1=1$; $\beta_1=0$, $g_1^j=\ln(\bar{\sigma})$ ($\alpha_2=0$, $\beta_2=1$ $g_n^j=\ln(\bar{\sigma})$). For impermeable top (bottom) boundary, $\alpha_1=\beta_1, g_1^j=0$ ($\alpha_2=\beta_2, g_n^j=0$). The numerical procedures for the consolidation analysis of the sand-clay mixtures are presented in Fig. 4.

Model evaluation

Model parameters

The proposed elastic visco-plastic model has eight principal parameters: two of them are related to the reference time line of the clay matrix, N_c and λ_c; κ_c corresponds to the instant time line of the clay matrix; A_c and ξ_c are intrinsic permeability parameters; Among the creep parameters, t_0 is the indicator for the beginning of the creep time and t_e (end of primary consolidation), and ψ_c denotes the creep coefficient of the clay matrix. ϑ is a structure parameter incorporating the evolution of inter-granular structure of sand skeleton. N_c, λ_c, κ_c, t_0, and ψ_c can be calibrated from an oedometer test of the pure clay. The calibration procedure follows that described in Yin and Graham (1994).

The calibration of the permeability parameters (A_c and ξ_c) and the structure parameter ϑ are given as follows: The permeability k_c is computed from the compressibility and consolidation curves of the pure clay matrix based on the following equation (Shi and Yin, 2018b):

$$k_c = \frac{\lambda_c c_v \gamma_w}{\sigma_c'} \tag{37}$$

where c_v=0.212h^2/t_{90} is the coefficient of consolidation of the pure marine clay, h is the height of the specimen, t_{90} (s) is the time duration at 90% of consolidation. The permeability parameters A_c and ξ_c can be calibrated from the permeability data points (k_c and e_c in double logarithmic plot) at different stress levels. As summarized by Shi and Yin (2018b), the ranges of the permeability parameters are -35~-22 for A_c and 3.5~6.7 for ξ_c. The structure parameter ϑ can be calibrated based on two oedometer tests: one on the pure clay and the other on the mixture with a predefined fraction of sand particles. It can be determined from the relationship between the structure variable η and the sand volume fraction ϕ_s. The value of the structure parameter ϑ for different soils varies within a narrow range, from 0.7 (low plasticity clay) to 0.8 (high plasticity clay).

Benchmark analysis of the model

This section presents benchmark examples for the consolidation analysis of mixtures, including both Eulerian and Lagrangian coordinates and their comparisons. The one in Eulerian coordinate can be regarded as an extended from the model proposed by Yin and Graham (1994), and the original model after Yin and Graham (1994) recovers if the sand fraction is reduced to 0. Other EVP models based on Hypothesis A, e.g., the ones proposed by Hinchberger et al. (2010) and Chang & Zoback (2010), may not be particularly suitable for coupling hydro-mechanical analysis of saturated sand-clay mixtures.

Consider a thin soil layer with a thickness of h =2cm subjected to a uniform surcharge loading on both the top surface (ζ =0) and the bottom surface ζ =h. Both surfaces are assumed to be free drain. The minimum void ratio of the sand material is 0.54, and the clay and sand particles are assumed to have the same density of 2650 kg/m^3. The model parameters are given in Table 1. The soil layer is discretized with 200 nodes, with a uniform initial effective stress of 5 kPa. The initial states of the mixtures are assumed to be on the reference time lines. Six steps of subsequent surcharge loading are applied: 5, 10, 25, 50, 100, 200 kPa. The state variables (excess pore water pressure, effective stress, and the stress ratio) at the middle of the soil layer are recorded during the simulation.

Fig. 5(a) shows the compression curves of the sand clay mixtures in terms of overall specific volume and overall effective stress in Eulerian coordinates. It is seen that the pattern of compression curves is different from the reference time lines. The compression curves are nonlinear due to the coupling of excess pore water dissipation and time dependent deformation. The local deformation of the mixtures is depicted in Fig. 5(b). The compression curves of the mixture gradually deviate from the corresponding ones of the pure clay with the increase of both sand mass fraction and stress level. This can be explained by the evolution of the incremental stress ratio in Fig. 6: the volume fraction of sand increases with sand mass fraction and stress level. Correspondingly, the incremental stress ratio decreases (refer to Eqs (19) and (20)), and the clay matrix shows a smaller compressibility.

The excess pore water pressure dissipation of the mixtures (loading increment of 100 kPa) is shown in Fig. 7 in a semi-logarithmic plot. For a low sand mass fraction (50%), the consolidation curve of the mixture is relatively close to the one of pure clay. However, the consolidation process is accelerated with further increase of the sand fraction. This is due to the different evolution of local stress in the clay matrix. As shown in Fig. 6, at the same surcharge loading the local stress in the clay matrix decreases with the sand fraction. Consequently, a higher local void ratio and higher permeability of the clay matrix can be expected for the mixture with a higher sand mass fraction, and this induces a more rapid pore water pressure dissipation.

The consolidation data (including the compression curves, excess pore water pressure dissipation, and stress ratio) of the mixtures in Lagrangian coordinates is presented in Figs 8-10. The compression curves and the incremental stress ratio evolution are approximately the same as the corresponding ones in Eulerian coordinates. Fig. 10 presents the excess pore water pressure dissipation at all loading steps. The consolidation curves with different sand fractions almost overlap at loading increments of 5 kPa, since the local stresses in the matrix are close, and the incremental stress ratio is higher than 0.9. With increasing stress level, the consolidation process is significantly affected by the sand fraction. The consolidation curves of the pure clay and mixture (υ_s=70%) are plotted in the same figures (Fig. 11), highlighting the difference caused by the use of the two coordinates. The soil skeleton of the mixtures and the boundaries are fixed to the Lagrangian coordinates. Therefore, the time dependent boundaries can be defined, and a more rapid dissipation of the excess pore water pressure can be expected due to decreasing thickness of the consolidating soil layer. The settlement of the pure clay and mixture (υ_s=70%) within Eulerian and Lagrangian coordinates are shown in Fig. 12 (loading increment of 100kPa). The final settlements are almost the same in the two cases. However, due to different rate of dissipation, the settlements are different during the primary consolidation process.

Validation of the model

Section 5 indicates the consolidation model in Lagrangian coordinates is more reasonable. It is adopted for comparison with the experimental data from literature. Two sand-clay mixtures exhibiting significantly different creep behavior are presented for the validation: (1) the sand-marine clay mixtures (data from Shi and Yin, 2018a) with small creep coefficient, and sand-bentonite mixtures (data from Shi *et al.*, 2018) showing a large creep deformation. The oedometer tests on the two mixtures follow the same procedure: First, water was added to the dry clay matrix to get slurries with desired initial water contents; The matrix slurry and sand particles were then mixed homogeneously for a given sand fraction; Finally, the sample was poured into a cutting ring, and the consolidation stress was increased stepwise. For more details of the test procedure, one can refer to Shi et al. (2018) and Shi & Yin (2018a).

Sand-bentonite mixtures

The mixture consists of bentonite matrix and silicon sand inclusions. The particle size of silicon sand ranges from 1.0 mm to 2.0 mm. The minimum void ratio of the sand material is 0.55. The particle densities of the constituents are 2690 and 2700 kg/m^3 for the sands and clay particles, respectively. Due to the extremely high liquid limit of the bentonite matrix, the initial water content of the clay matrix is as high as 885%. Mixtures with four different sand fractions (0%, 50%, 65%, 75%) were tested. The time duration at a given stress level is more than 5000 mins, the loading period is more than 10000 mins at the consolidation stress of 100 kPa. The creep coefficient of the bentonite matrix shows a significant variation within the test stress range. It can be approximated by a function of the effective stress (Fig. 13):

$$\psi_c = 0.92\left(\frac{\sigma'_c}{\sigma_r}\right)^{-0.5} \tag{38}$$

Note that the effective stress σ'_c is the average stress of the initial and final values a given consolidation stress.

Sand-marine clay mixtures

The data of the sand-marine clay matrix follow those presented by Shi and Yin (2018a). The mixture is composed of Hong Kong Marine Deposits and a coarse sand material, with four sand mass fractions (0%, 20%, 40%, 60%). The minimum void ratio of sands is 0.601. The liquid limit of the marine clay is 62.4%, and the initial water content of the clay matrix is 86.9%. The particle densities of the sand and clay matrix are 2630 and 2680 kg/m^3, respectively. The parameter t_0 related to the reference time line is 100 mins. The creep coefficient of the marine clay matrix varies within a narrow range (0.005-0.009), thus an average value of 0.007 has been adopted for the simulation.

Evaluation of the model

The data at small stress levels (blew 5 kPa) are excluded from analysis. Following the laboratory testing in Shi and Yin (2018a), both the top and bottom surfaces are assumed to be free draining. A uniform initial stress of 5 kPa is assumed. The model parameters for the sand-marine clay matrix and sand bentonite matrix are listed in Table 1. The model parameter $t_0 = 1440$ min. The initial void ratios of the bentonite and marine clay matrix are 16.57 and 2.02, respectively. The overall void ratios of the sand-marine clay mixtures are 1.61, 1.20 and 0.80 for the sand fractions of 20%, 40% and 60%, respectively (The values for sand-bentonite mixtures are 8.27, 5.79 and 4.13 for the sand fractions of 50%, 65% and 75%). The discretized domain contains 201 nodes, with a surcharge loading of 5.0 kPa applied on the top surface, followed by the loading steps of 10, 25, 50, 100, 200, and 400 kPa.

Figs 14 and 16 present a comparison between the experimental data and the model simulations in the semilogarithmic compression plane $v:\ln\sigma'$ (based on Lagrangian coordinate). The compression data are associated with the reference time lines, and the simulated curves corresponds to the equivalent time less than zero. The final simulated results agree well with the experimental data. The simulated consolidation curves based on Lagrangian coordinate at different stress levels are shown in Figs 15 and 17 in terms of the consolidation time and overall strain in the current loading step. It is seen that the effect of sand fraction on the consolidation behavior of the sand-clay mixtures can be well reproduced by the proposed model. The simulation consolidation curves based on Eulerian coordinate are also provided for comparison (see Fig. 18 for the simulated results and test data of the sand-bentonite mixtures).

To assess the capability of the proposed models, the simulated curves are compared against the measured strain to examine the relative errors. The relative error (*RE*) is defined as (see Fig. 19):

$$RE = \frac{\sum_{i=1}^{N} \left| \varepsilon_{model} - \varepsilon_{test} \right|}{\sum_{i=1}^{N} \varepsilon_{test}} \tag{38}$$

where ε_{model} is the overall strain of the mixture computed from the models, ε_{test} is the overall strain from interpolation of the test data, N is the number of equidistance points sampled from the consolidation curves (14 points are used in this work for calculation of the relative error). The relative errors of the proposed models are shown in Fig. 20. The relative error of the EVP model based on Lagrangian coordinate is significantly lower than that based on Eulerian coordinate, and the difference increases with the effective stress level. This is due to the decrease of the thickness of the samples, which cannot be incorporated into the model using Eulerian coordinate.

Previous EVP models have been proposed for a soil with a predefined composition. For sand-clay mixtures, the model parameters based on classical EVP models have to change with the sand fraction. These models have several drawbacks: (1) To correlate the model parameters with the sand mass fractions, one must perform many oedometer tests on sand-clay mixtures with a wide range of sand fractions, which is time-consuming. (2) Empirical equations used for the above correlations are based on mass fraction of sand. However, the model parameters should depend on the volume fraction of sand, which changes during the consolidation process; (3) The empirical correlation will introduce additional parameters which do not always have concrete physical meanings. The proposed model in this study overcomes the above shortcomings. Only two multi-stage oedometer tests (including unloading stages) need to be performed for calibrating the model parameters, which makes the model more suitable for the field analysis by engineers.

Conclusions

A new elastic visco-plastic (EVP) model considering both small and finite strains was proposed for the time dependent stress-strain behavior of sand-clay mixtures. The EVP model has been applied in a one-dimensional (1D) finite strain consolidation analysis of mixtures, is further benchmarked and validated, using a finite difference method. The following conclusions are drawn:

(1) Our new 1D EVP model simulation results reveal that the sand fraction significantly affects the pore water dissipation in a sand-clay mixture. This is indeed consistent with the fact that the rate of consolidation becomes faster with the increase of sand fraction which causes higher local void ratio and higher permeability of the mixture.

(2) Benchmark analysis of the proposed model in a 1D consolidation analysis reveals that the

dissipation of the excess pore water pressure using Lagrangian coordinate is more rapid than the one based on Eulerian coordinate due to the decreasing thickness of the consolidating soil layer.

(3) The proposed 1D EVP model has eight parameters. The structure parameter responsible for the inter-granular structure can be calibrated based on the reference time line of the mixture with a predefined sand fraction. The other parameters can be derived from the compressibility and consolidation curves of the clay matrix.

(4) Experimental data of sand-bentonite mixtures and sand-marine clay mixtures have been used for validation of the proposed model. The sand fraction effects can be well reproduced by the proposed model in Lagrangian coordinates.

Acknowledgement

The work in this paper is partially supported by a National State Key Project "973" grant (Grant No.: 2014CB047000) (sub-project No. 2014CB047001) from Ministry of Science and Technology of the People's Republic of China, a CRF project (Grant No.: PolyU12/CRF/13E) and a Theme-based Research Scheme (Grant No: T22-603/15-N) from Research Grants Council (RGC) of Hong Kong Special Administrative Region Government (HKSARG) of China, two GRF projects (PolyU 152196/14E; PolyU 152796/16E) from RGC of HKSARG of China. The authors also acknowledge the financial supports from Research Institute for Sustainable Urban Development of The Hong Kong Polytechnic University, grants (1-ZVCR, 1-ZVEH, 4-BCAU, 4-BCAW, 5-ZDAF, G-YN97) from The Hong Kong Polytechnic University.

Appendix-1: derivation of the governing equation (Eq. (28))

Combining Eqs (13), (14), (26), and (27), one obtains:

$$\frac{(1+e_0)^2}{(1+e)m_v}\frac{\partial}{\partial\zeta}\left(\frac{k_c}{\gamma_w(1+e)}\frac{\partial p}{\partial\zeta}\right)=(1-\phi_s)\mu_\sigma^c\frac{\partial p}{\partial t}-(1-\phi_s)\frac{\sigma'_c\psi_c}{\kappa_c t_0}\exp\left(\frac{v_c-N_c}{\psi_c}\right)\left(\frac{\sigma'_c}{\sigma_r}\right)^{\frac{\lambda_c}{\psi_c}} \quad \text{(A1)}$$

Considering the effective stress concept, it follows

$$\frac{(1+e_0)^2}{(1+e)m_v}\frac{\partial}{\partial\zeta}\left(\frac{\sigma' k_c}{\gamma_w(1+e)}\frac{\partial\ln(\sigma')}{\partial\zeta}\right)=(1-\phi_s)\sigma'\mu_\sigma^c\frac{\partial\ln(\sigma')}{\partial t}+(1-\phi_s)\frac{\sigma'_c\psi_c}{\kappa_c t_0}\exp\left(\frac{v_c-N_c}{\psi_c}\right)\left(\frac{\sigma'_c}{\sigma_r}\right)^{\frac{\lambda_c}{\psi_c}} \quad \text{(A2)}$$

$\frac{\sigma' k_c}{\gamma_w(1+e)}$ is closely related to the coefficient of consolidation which is approximately constant for a stress increment during consolidation process. Hence, Eq. (A2) is rearranged as

$$\frac{(1+e_0)^2 k_c}{(1+e)^2\gamma_w m_v}\frac{\partial}{\partial\zeta}\left(\frac{\partial\ln(\sigma')}{\partial\zeta}\right)=(1-\phi_s)\mu_\sigma^c\frac{\partial\ln(\sigma')}{\partial t}+(1-\phi_s)\frac{\sigma'_c\psi_c}{\sigma'\kappa_c t_0}\exp\left(\frac{v_c-N_c}{\psi_c}\right)\left(\frac{\sigma'_c}{\sigma_r}\right)^{\frac{\lambda_c}{\psi_c}} \quad \text{(A3)}$$

References

Anderson, M. T., & Lu, N. (2001). Role of microscopic physicochemical forces in large volumetric strains for clay sediments. *Journal of engineering mechanics*, 127(7), 710-719.

Bian, X., Cao, Y. P., Wang, Z. F., Ding, G. Q., & Lei, G. H. (2017). Effect of super-absorbent polymer on the undrained shear behavior of cemented dredged clay with high water content. *Journal of Materials in Civil Engineering*, 29(7), 04017023.

Bian, X., Wang, Z. F., Ding, G. Q., & Cao, Y. P. (2016). Compressibility of cemented dredged clay at high water content with super-absorbent polymer. *Engineering Geology*, 208, 198-205.

Bjerrum, L. (1967). Engineering geology of Norwegian normally-consolidated marine clays as related to settlements of buildings. *Géotechnique*, 17(2), 83-118.

Borja, R. I., & Choo, J. (2016). Cam-Clay plasticity, Part VIII: A constitutive framework for porous materials with evolving internal structure. *Computer Methods in Applied Mechanics and Engineering*, 309, 653-679.

Borja, R. I., & Koliji, A. (2009). On the effective stress in unsaturated porous continua with double porosity. *Journal of the Mechanics and Physics of Solids*, 57(8), 1182-1193.

Chang, C., & Zoback, M. D. (2010). Viscous creep in room-dried unconsolidated Gulf of Mexico shale (II): Development of a viscoplasticity model. Journal of Petroleum Science and Engineering, 72(1-2), 50-55.

Chang, W. J., Chang, C. W., & Zeng, J. K. (2014). Liquefaction characteristics of gap-graded gravelly soils in K_0 condition. *Soil Dynamics and Earthquake Engineering*, 56, 74-85.

Choo, J., & Borja, R. I. (2015). Stabilized mixed finite elements for deformable porous media with double porosity. *Computer Methods in Applied Mechanics and Engineering*, 293, 131-154.

Cui, Y., Chan, D., & Nouri, A. (2017a). Coupling of solid deformation and pore pressure for undrained deformation-a discrete element method approach. *International Journal for Numerical and Analytical Methods in Geomechanics*, 41(18), 1943-1961.

Cui, Y., Chan, D., & Nouri, A. (2017b). Discontinuum modeling of solid deformation pore-water diffusion coupling. *International Journal of Geomechanics,* 17(8), 4017033.

Cui, Y., Choi, C. E., Liu, L. H. D., & Ng, C. W. W. (2018). Effects of Particle Size of Monodispersed Granular Flows Impacting a Rigid Barrier. *Natural Hazards*, 91(3), 1179-1201.

Cui, Y., Nouri, A., Chan, D., & Rahmati, E. (2016). A new approach to DEM simulation of sand production. *Journal of Petroleum Science and Engineering*, 147, 56-67.

Cui Y. F., Zhou X. J., & Guo C. X. (2017). Experimental study on the moving characteristics of fine grains in wide grading unconsolidated soil under heavy rainfall. *Journal of Mountain Science*, 14(3), 417-431.

Deng, Y., Wu, Z., Cui, Y., Liu, S., & Wang, Q. (2017). Sand fraction effect on hydro-mechanical behavior of sand-clay mixture. *Applied Clay Science*, 135, 355-361.

Dolinar, B. (2009). Predicting the hydraulic conductivity of saturated clays using plasticity-value correlations. *Applied Clay Science*, 45(1), 90-94.

Feng, S. J., Zhang, X., & Cao, B. Y. (2014). Leachate recirculation in bioreactor landfills considering the effect of MSW settlement on hydraulic properties. *Environmental Earth Sciences*, 72(7), 2315-2323.

Gibson, R. E., England, G. L., & Hussey, M. J. L. (1967). The Theory of one-dimensional consolidation of saturated clays: 1. finite non-Linear consolidation of thin homogeneous layers. *Géotechnique*, 17(3), 261-273.

González, C., Segurado, J., & LLorca, J. (2004). Numerical simulation of elasto-plastic deformation of composites: evolution of stress microfields and implications for homogenization models. *Journal of the Mechanics and Physics of Solids*, 52(7), 1573-1593.

Graham, J., Saadat, F., Gray, M. N., Dixon, D. A., & Zhang, Q. Y. (1989). Strength and volume change behaviour of a sand-bentonite mixture. Canadian Geotechnical Journal, 26(2), 292-305.

Hashin, Z. (1983). Analysis of composite materials-a survey. *Journal of Applied Mechanics*, 50(3), 481-505.

Hawlader, B. C., Muhunthan, B., & Imai, G. (2003). Viscosity effects on one-dimensional consolidation of clay. *International Journal of Geomechanics*, 3(1), 99-110.

He, B., Mortazavi, B., Zhuang, X., & Rabczuk, T. (2016). Modeling Kapitza resistance of two-phase composite material. *Composite Structures*, 152, 939-946.

Hinchberger, S. D., Qu, G., & Lo, K. Y. (2010). Constitutive approach for rate-sensitive anisotropic structured clays. *International Journal for Numerical and Analytical Methods in Geomechanics*, 34(17), 1797-1830.

Hong, Z., Yin, J., & Cui, Y. J. (2010). Compression behavior of reconstituted soils at high initial water contents. *Géotechnique*, 60(9), 691-700.

Horpibulsuk, S., Liu, M. D., Zhuang, Z., & Hong, Z. S. (2016). Complete compression curves of reconstituted clays. *International Journal of Geomechanics*, 16(6).

Huang, J., Xie, X., Zhang, J., Li, J., & Wang, W. (2014). Nonlinear Finite Strain Consolidation Analysis with Secondary Consolidation Behavior. *Mathematical Problems in Engineering*, 2014.

Hubert, J., Liu, X. F., & Collin, F. (2016). Numerical modeling of the long-term behavior of Municipal Solid Waste in a bioreactor landfill. *Computers and Geotechnics*, *72*, 152-170.

Imai, G., Tanaka, Y., & Saegusa, H. (2003). One-dimensional consolidation modeling based on the isotach law for normally consolidated clays. *Soils and Foundations*, 43(4), 173-188.

Kumar, G. V. (1996). Some aspects of the mechanical behavior of mixtures of kaolin and coarse sand (*Doctoral dissertation, University of Glasgow*).

Marques, A. C. M., Filz, G. M., & Vilar, O. M. (2003). Composite compressibility model for municipal solid waste. *Journal of Geotechnical and Geoenvironmental Engineering*, 129(4), 372-378.

Mesri, G. (2003). Primary compression and secondary compression. In *Soil behavior and soft ground construction* (pp. 122-166).

Mesri, G., & Castro, A. (1987). Cα/Cc concept and K0 during secondary compression. *Journal of Geotechnical Engineering*, 113(3), 230-247.

Mesri, G., & Godlewski, P. M. (1977). Time and stress compressibility interrelationship. *Journal of Geotechnical and Geoenvironmental Engineering*, 103 (ASCE 12910).

Mesri, G., and Olson, R. E. (1971). Mechanisms controlling the permeability of clays. *Clays Clay Minerals*, 19(3), 151-158.

Mitchell, J. K. 1993, Fundamentals of Soil Behavior, *John Wiley and Sons*, Inc., New York.

Monkul, M. M., & Ozden, G. (2005). Effect of intergranular void ratio on one-dimensional compression behavior. In *Proceedings of International Conference on Problematic Soils*, International Society of Soil Mechanics and Geotechnical Engineering, Famagusta, Turkish Republic of Northern Cyprus (Vol. 3, pp. 1203-1209).

Monkul, M. M., & Ozden, G. (2007). Compressional behavior of clayey sand and transition fines content. *Engineering Geology*, 89(3), 195-205.

Ng, T. T., Zhou, W., & Chang, X. L. (2016). Effect of particle shape and fine content on the behavior of binary mixture. *Journal of Engineering Mechanics*, 143(1), C4016008.

Pane, V., and Schiffman, R. L. (1997). The permeability of clay suspensions. *Géotechnique*, 47(2), 273–288.

Puppala, A. J., Pedarla, A., Pino, A., & Hoyos, L. R. (2017). Diffused Double-Layer Swell Prediction Model to Better Characterize Natural Expansive Clays. *Journal of Engineering Mechanics*, 143(9), 04017069.

Quayum, M. S., Zhuang, X., & Rabczuk, T. (2015). Computational model generation and RVE design of self-healing concrete. *Frontiers of Structural and Civil Engineering*, 9(4), 383-396.

Satyanaga, A., Rahardjo, H., Leong, E. C., & Wang, J. Y. (2013). Water characteristic curve of soil with bimodal grain-size distribution. *Computers and Geotechnics*, 48, 51-61.

Shi, X. S., & Herle, I. (2015). Compression and undrained shear strength of remoulded clay mixtures. *Géotechnique Letters*, 5(2), 62-67.

Shi, X. S., & Herle, I. (2017). Numerical simulation of lumpy soils using a hypoplastic model. *Acta Geotechnica*, 12(2), 349-363.

Shi, X. S., Herle, I., & Muir Wood, D. (2018). A consolidation model for lumpy composite soils in open-pit mining. *Géotechnique*, 68(3), 189-204.

Shi, X. S., & Yin, J. (2017). Experimental and theoretical investigation on the compression behavior of sand-marine clay mixtures within homogenization framework. *Computers and Geotechnics*, 90, 14-26.

Shi, X. S., & Yin, J. (2018a). Consolidation Behavior for Saturated Sand-Marine Clay Mixtures Considering the Intergranular Structure Evolution. *Journal of Engineering Mechanics*,144(2), 04017166.

Shi, X. S., & Yin, J. (2018b). Estimation of Hydraulic Conductivity of Saturated Sand–Marine Clay Mixtures with a Homogenization Approach. *International Journal of Geomechanics*, 18(7), 04018082.

Shi, X.S., Yin, J. H, Feng, W.Q. & Chen, W.B. (2018) Analysis of the creep coefficient of binary sand-bentonite mixtures in oedometer condition using mixture theory. *International Journal of Geomechanics* (In press).

Silva, S. D. Three runway system project (3RS project), contract 3206-main reclamation works. *Report for ZHECC-CCCC-CDC joint venture*. 7076481/R00: Hong Kong, 2016.

Singh, R. P., Singh, M., & Ojha, C. P. (2014). An experimental study on consolidation of compacted clays. *International Journal of Geotechnical Engineering*, 8(1), 112-117.

Tu, S. T., Cai, W. Z., Yin, Y., & Ling, X. (2005). Numerical simulation of saturation behavior of physical properties in composites with randomly distributed second-phase. *Journal of composite materials*, 39(7), 617-631.

Valliappan, S., & Khalili-Naghadeh, N. (1990). Flow through fissured porous media with deformable matrix. *International journal for numerical methods in engineering*, 29(5), 1079-1094.

Weng, G. J., & Tandon, G. P. (1988). A theory of particle-reinforced plasticity. *ASME Journal of Applied Mechanics*, 55(3), 126-135.

Xie, K. H., & Leo, C. J. (2004). Analytical solutions of one-dimensional large strain consolidation of saturated and homogeneous clays. *Computers and Geotechnics*, 31(4), 301-314.

Yin, J. H. (1999a). Non-linear creep of soils in oedometer tests. *Géotechnique*, 49(5), 699-707.

Yin, J. H. (1999b). Properties and behavior of Hong Kong marine deposits with different clay contents. *Canadian Geotechnical Journal*, 36(6), 1085-1095.

Yin, J. H., & Feng, W. Q. (2017). A new simplified method and its verification for calculation of consolidation settlement of a clayey soil with creep. *Canadian Geotechnical Journal*, 54(3), 333-347.

Yin, J. H., & Graham, J. (1994). Equivalent times and one-dimensional elastic viscoplastic modelling of time-dependent stress-strain behaviour of clays. *Canadian Geotechnical Journal*, 31(1), 42-52.

Yin, J. H., and Graham, J. (1996). Elastic visco-plastic modelling of one-dimensional consolidation. *Géotechnique*, 46(3): 515-527.

Zeng, L. L., Hong, Z. S., Cai, Y. Q., & Han, J. (2011). Change of hydraulic conductivity during compression of undisturbed and remolded clays. *Applied Clay Science*, 51(1-2), 86-93.

Zeng, L. L., Hong, Z. S., & Chen, F. Q. (2012). A law of change in permeability coefficient during compression of remolded clays. Rock and Soil Mechanics,33(5), 1286-1292.

Zeng, L. L., Hong, Z. S., & Cui, Y. J. (2015). Determining the virgin compression lines of reconstituted clays at different initial water contents. *Canadian Geotechnical Journal*, 52(9), 1408-1415.

Zeng, L. L., Hong, Z. S., & Cui, Y. J. (2016). Time-dependent compression behaviour of dredged clays at high water contents in China. *Applied Clay Science*, 123, 320-328.

Zhao, M., Zhang, Q., Li, S., & Zhao, H. (2017). Investigation on coupled fluid-flow and stress in dual model rock mass with time-dependent effect and its simulation. *Geosciences*, 7(3), 45.

Zhou, Z., Yang, H., Wang, X., & Liu, B. (2016). Model development and experimental verification for permeability coefficient of soil-rock mixture. *International Journal of Geomechanics*, 17(4), 04016106.

Zhuang, X., Huang, R., Liang, C., & Rabczuk, T. (2014). A coupled thermo-hydro-mechanical model of jointed hard rock for compressed air energy storage. *Mathematical Problems in Engineering*.

Zhuang, X., Wang, Q., & Zhu, H. (2015). A 3D computational homogenization model for porous material and parameters identification. *Computational Materials Science*, 96, 536-548.

Zhuang, X., Wang, Q., & Zhu, H. (2017). Effective properties of composites with periodic random packing of ellipsoids. *Materials*, 10(2), 112.

Table 1. Model parameters for benchmark analysis and validation of the proposed model

Parameters	Benchmark analysis	Sand-bentonite	Sand-marine clay
N_c	20	22	3.33
λ_c	2.50	2.75	0.22
κ_c	1.0	0.94	0.07
t_0 (min)	1440	1440	100
ψ_c	0.10	Eq. (37)	0.007
A_c	-30.0	-34.0	-22.7
ξ_c	4.00	4.18	4.15
ϑ	0.80	0.80	0.75

List of Figures

Figure 1. Schematic figure of equivalent time lines for clay matrix in sand-clay mixtures

Figure 2. Illustration of nonuniform state variables in binary sand-clay mixtures

Figure 3. Configuration for finite difference analysis

Figure 4. Flow chart for the consolidation analysis of sand-clay mixtures using Finite Difference Method

Figure 5. Consolidation analysis of sand-clay mixtures within Eulerian coordinate: (a) overall specific volume, (b) local specific volume

Figure 6. Evolution of stress ratio in oedometer compression (middle of the sample) within Eulerian coordinate

Figure 7. Evolution of excess pore water pressure (middle of the sample) within Eulerian coordinate (100-200 kPa)

Figure 8. Consolidation analysis of sand-clay mixtures within Lagrangian coordinate: (a) overall specific volume, (b) local specific volume

Figure 9. Evolution of stress ratio in oedometer compression (middle of the sample) within Lagrangian coordinate

Figure 10. Evolution of excess pore water pressure at different stress levels (middle of the sample) within Lagrangian coordinate: (a) pore water pressure increments of 5 kPa, 15 kPa and 25 kPa, (b) pore water pressure increments of 50 kPa, 100 kPa and 200 kPa

Figure 11. Evolution of excess pore water pressure within Eulerian and Lagrangian coordinates (100-200 kPa): (a) $\upsilon_s = 0$ %, (b) $\upsilon_s = 70$ %

Figure 12. Settlement of the sand-clay mixtures within Eulerian and Lagrangian coordinates (100-200 kPa): (a) $\upsilon_s = 0$ %, (b) $\upsilon_s = 70$ %

Figure 13. Change of creep coefficient of bentonite matrix

Figure 14. Comparison between the experimental data and the model simulation in v-σ' compression plane (sand-bentonite mixtures)

Figure 15. Comparison between the experimental data and the model simulation based on Lagrangian coordinate (sand-bentonite mixtures): (a) 5-10 kPa, (b) 10-25 kPa, (c) 25-50 kPa, (d) 50-100 kPa, (d) 100-200 kPa

Figure 16. Comparison between the experimental data and the model simulation in v-σ' compression plane (sand-marine clay mixtures)

Figure 17. Comparison between the experimental data and the model simulation based on Lagrangian coordinate (sand-marine clay mixtures): (a) 5-10 kPa, (b) 10-25 kPa, (c) 25-50 kPa, (d)

50-100 kPa, (d) 100-200 kPa, (e) 200-400 kPa

Figure 18. Comparison between the experimental data and the model simulation based on Eulerian coordinate (sand-bentonite mixtures) (a) 5-10 kPa, (b) 10-25 kPa, (c) 25-50 kPa, (d) 50-100 kPa, (d) 100-200 kPa

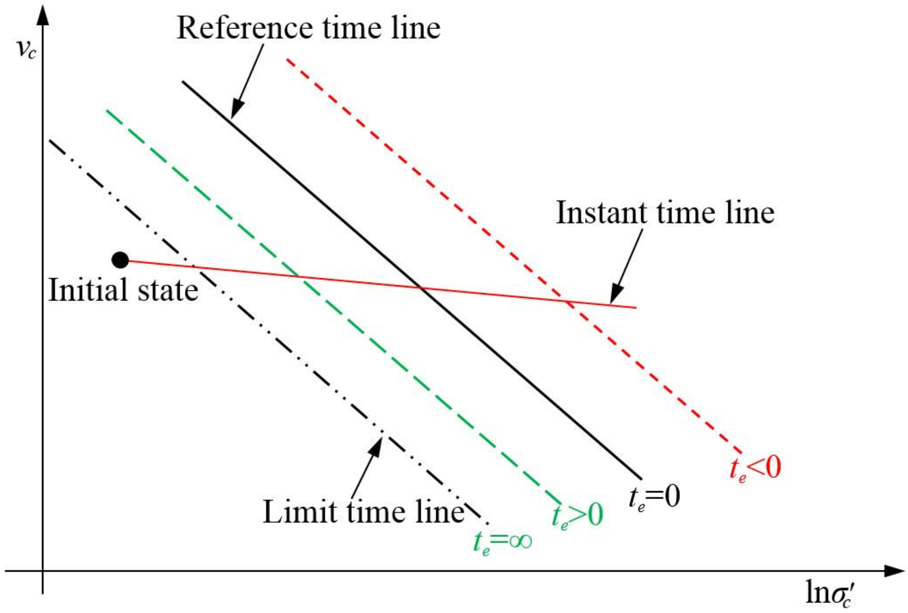

Figure 1: Schemetric figure of equivalent time lines for clay matrix in sand-clay mixtures

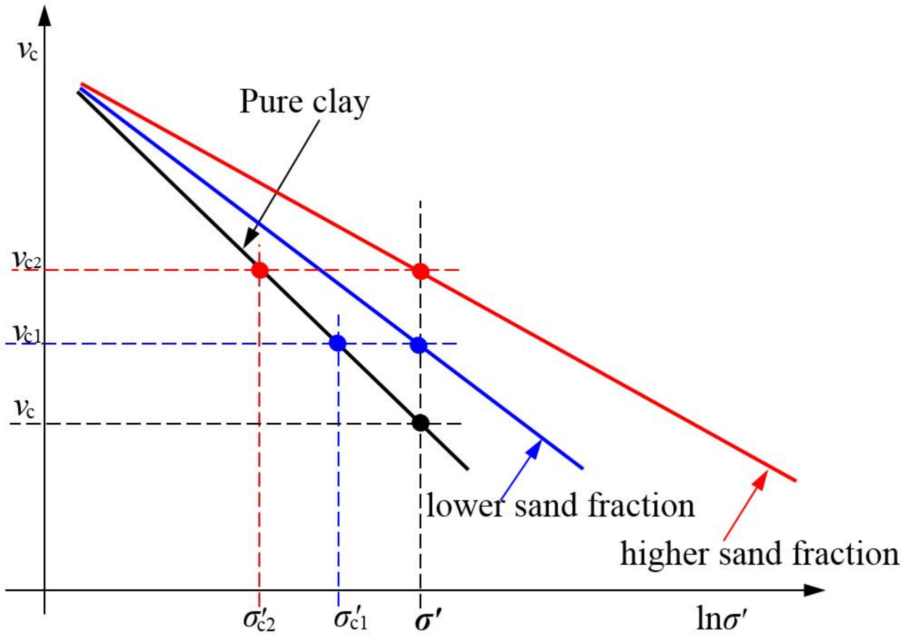

Figure 2: Illustration of nonuniform state variables in binary sand-clay mixtures

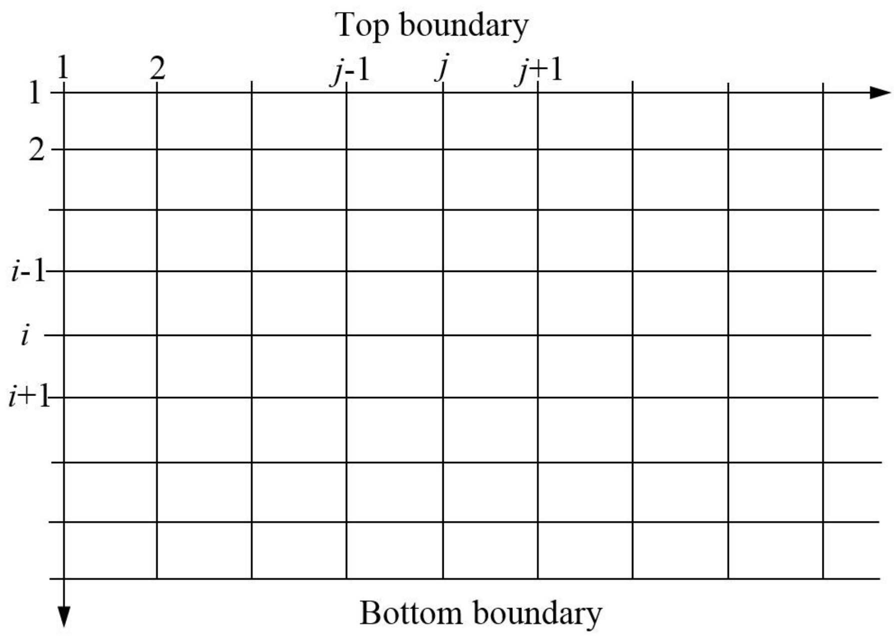

Figure 3: Configuration for finite difference analysis

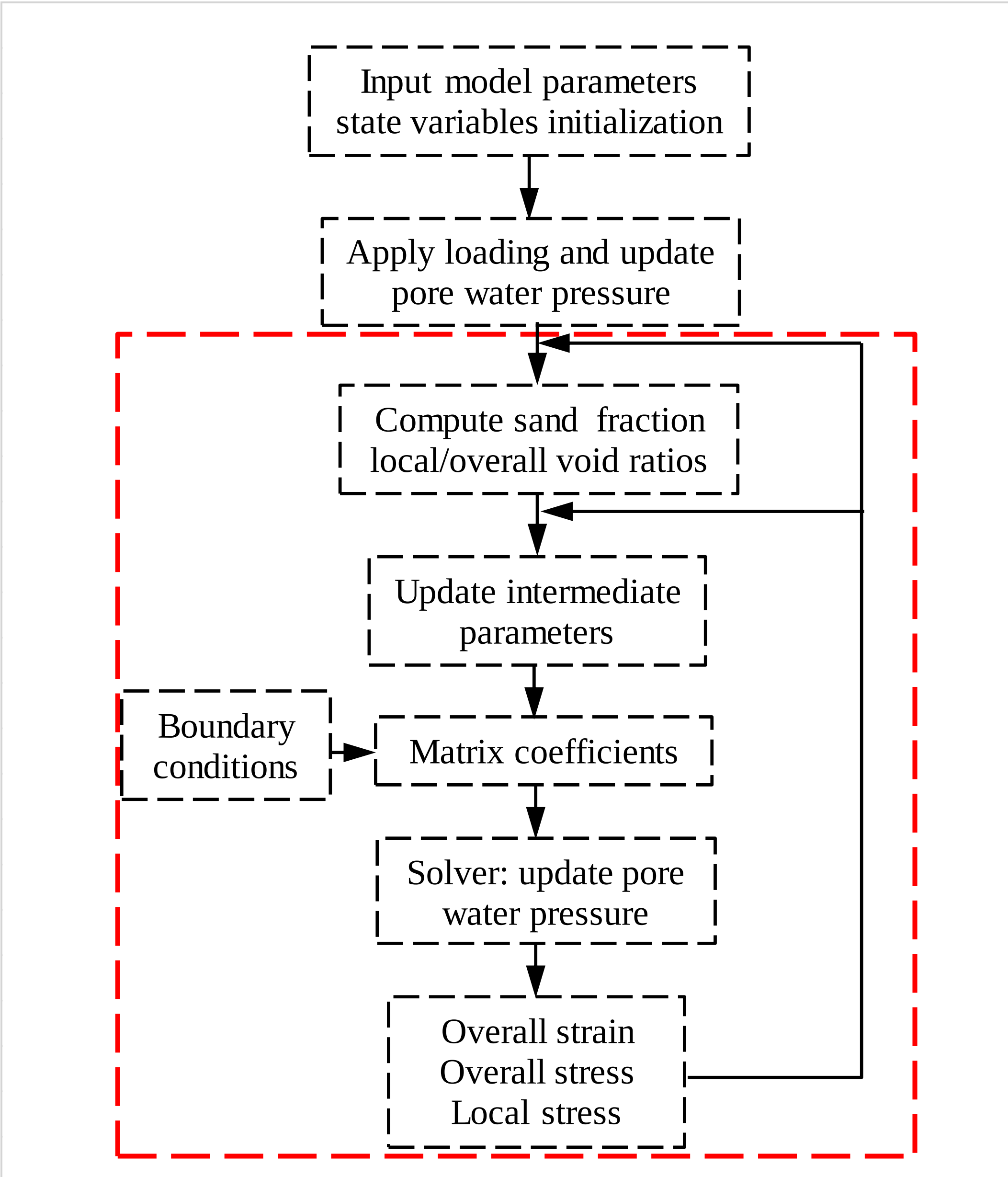

Figure 4: Flow chart for the consolidation analysis of sand-clay mixtures using Finite Difference Method

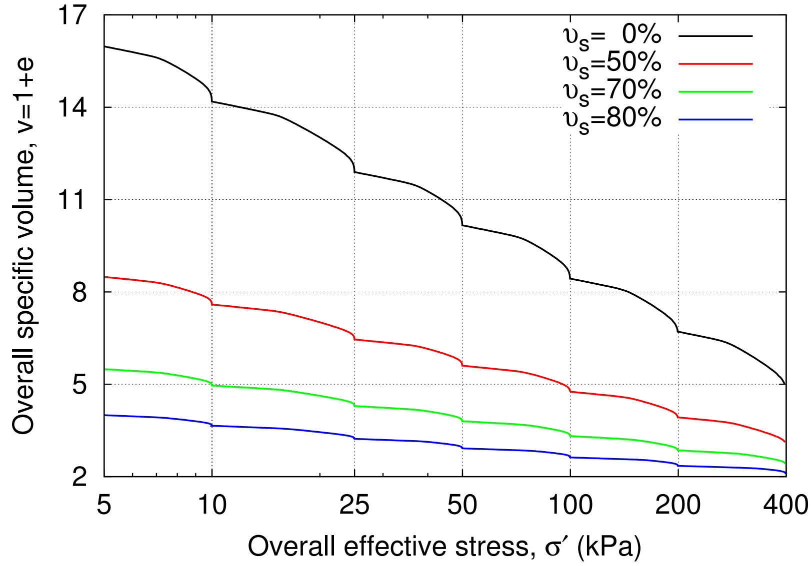

(a) Overall specific volume

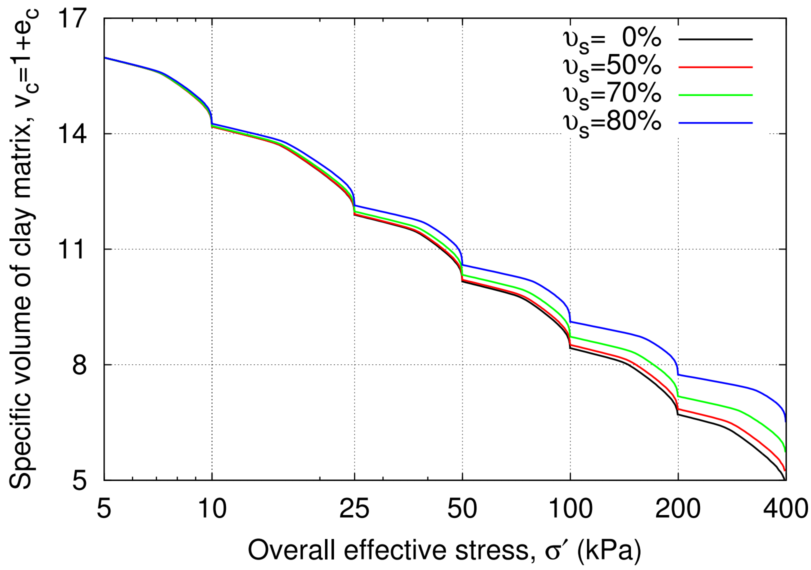

(b) Local specific volume

Figure 5: Consolidation analysis of sand-clay mixtures within Eulerian coordinate

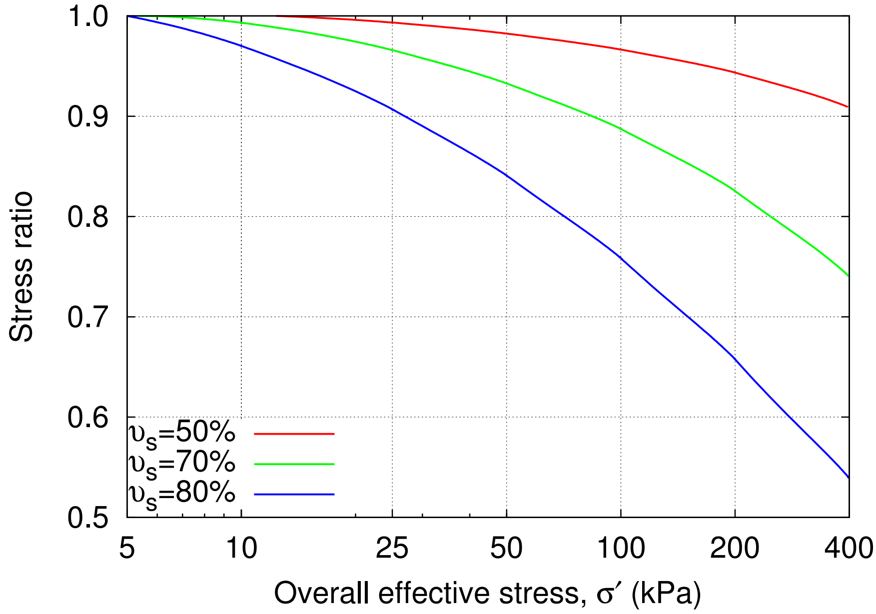

Figure 6: Evolution of stress ratio in oedometer compression (middle of the sample) within Eulerian coordinate

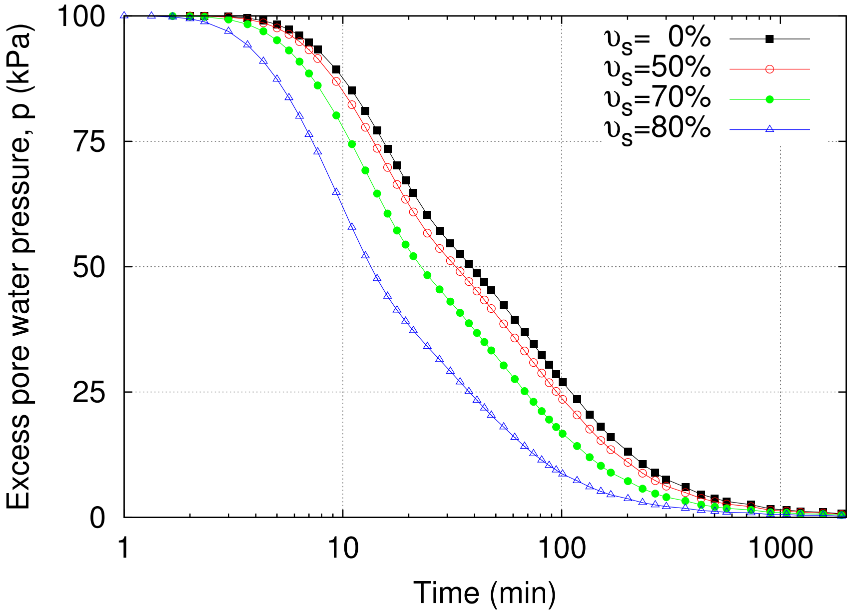

Figure 7: Evolution of excess pore water pressure (middle of the sample) within Eulerian coordinate (100-200 kPa)

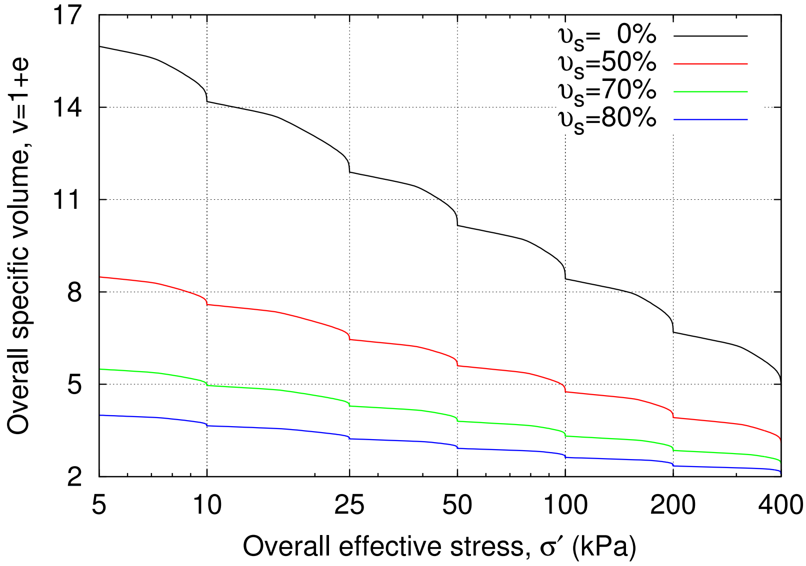

(a) Overall specific volume

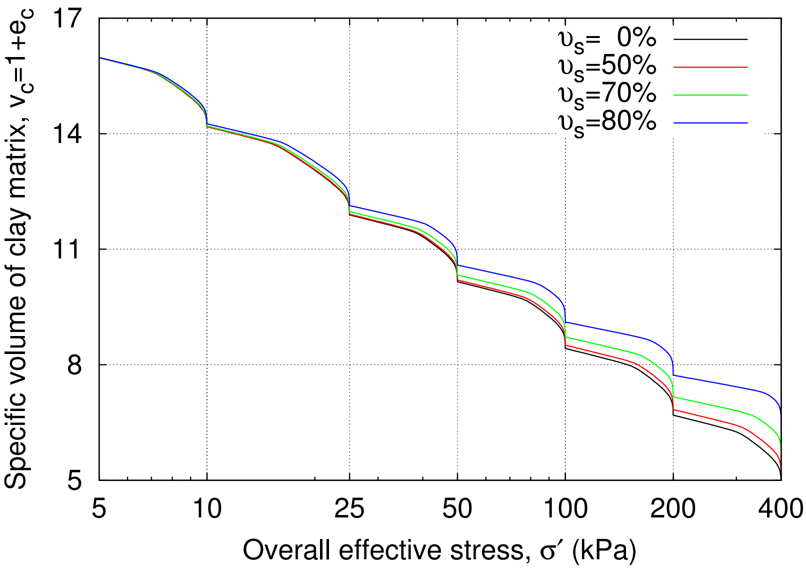

(b) Local specific volume

Figure 8: Consolidation analysis of sand-clay mixtures within Lagrangian coordinate

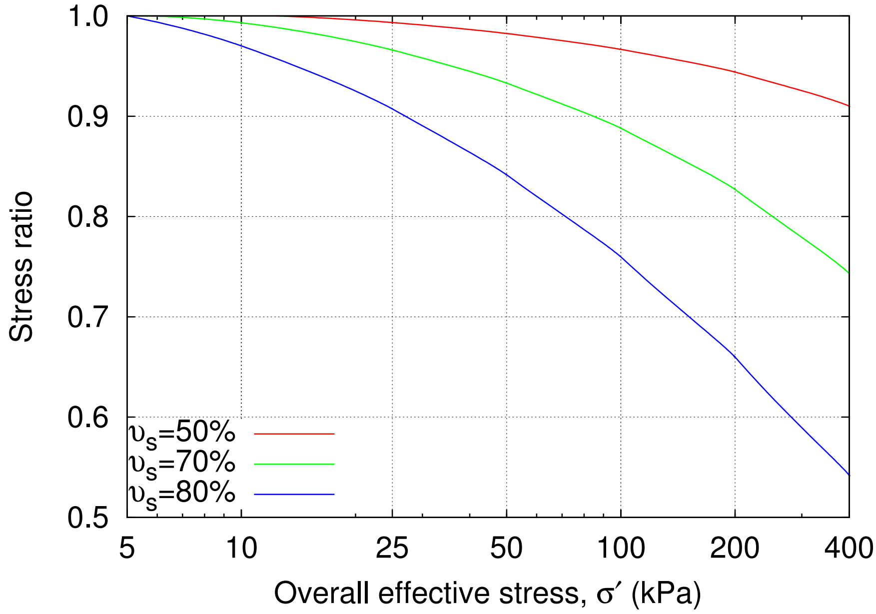

Figure 9: Evolution of stress ratio in oedometer compression (middle of the sample) within Lagrangian coordinate

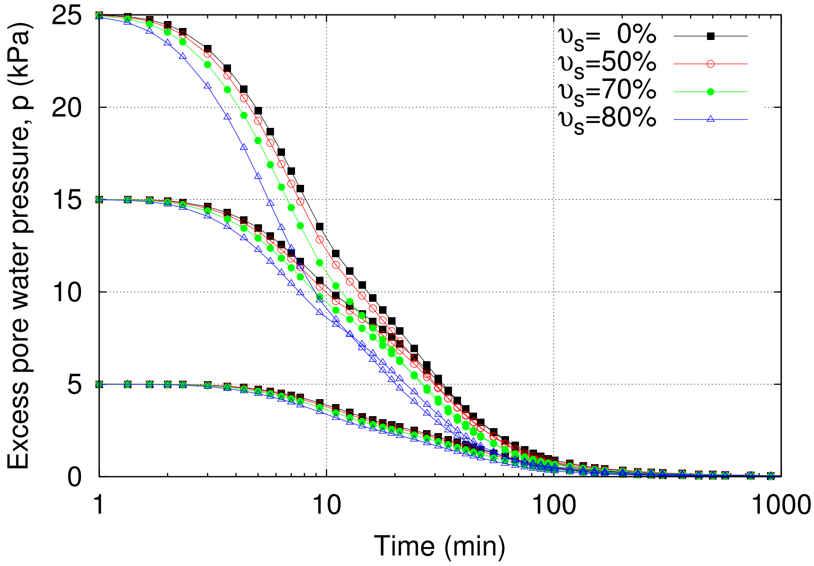

(a) Pore water pressure increments of 5 kPa, 15 kPa and 25 kPa

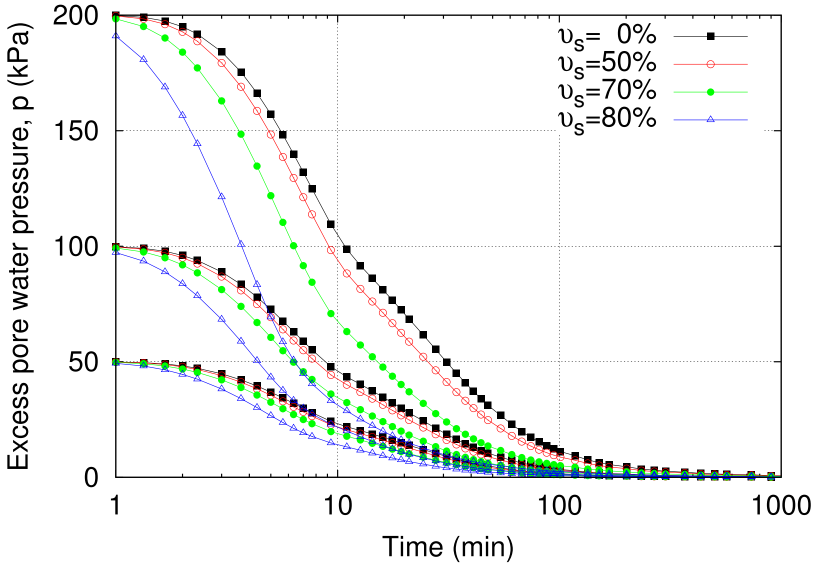

(b) Pore water pressure increments of 50 kPa, 100 kPa and 200 kPa

Figure 10: Evolution of excess pore water pressure at different stress levels (middle of the sample) within Lagrangian coordinate

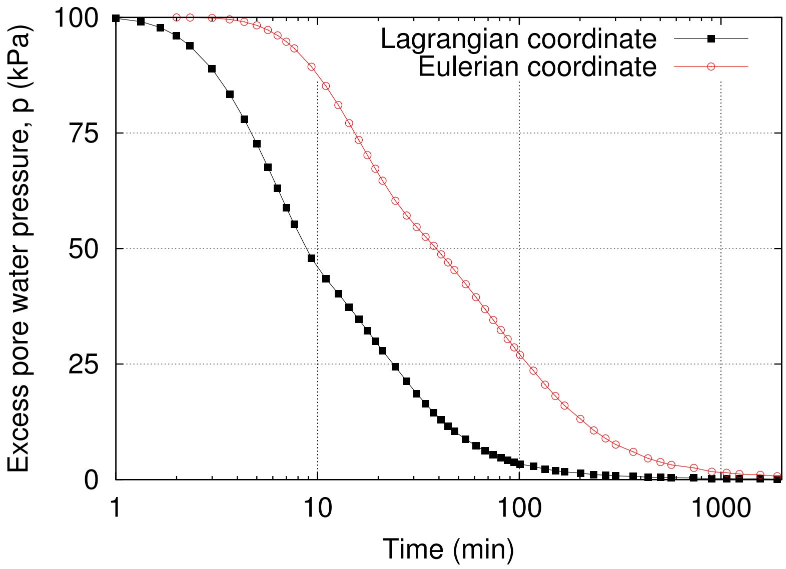

(a) $\upsilon_s = 0$ %

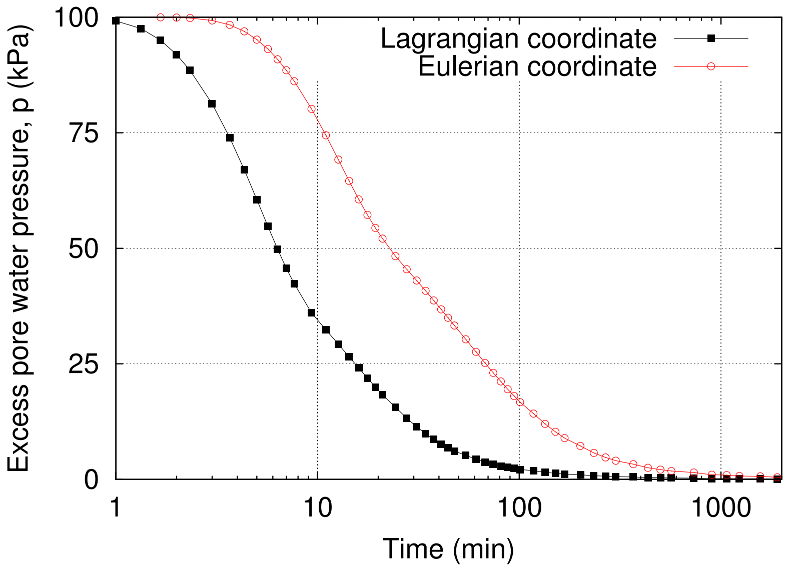

(b) υ_s =70 %

Figure 11: Evolution of excess pore water pressure within Eulerian and Lagrangian coordinates (100-200 kPa)

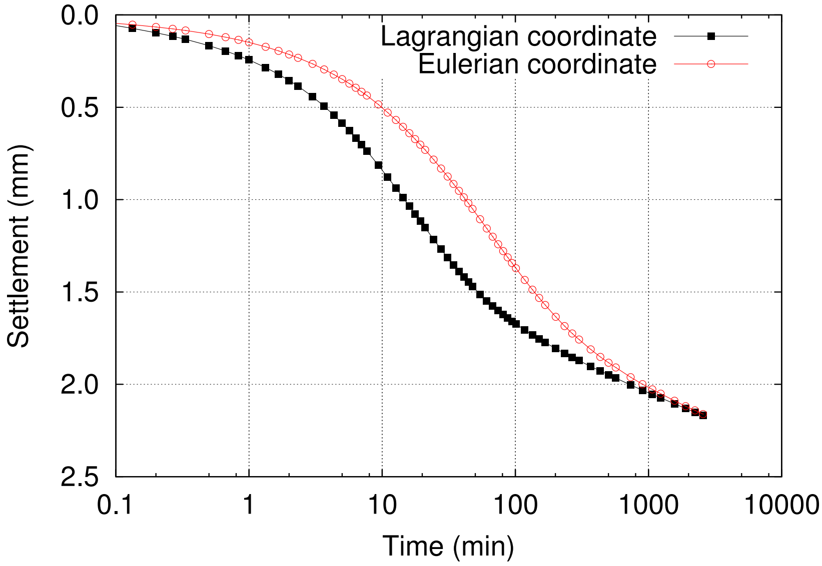

(a) $\upsilon_s = 0$ %

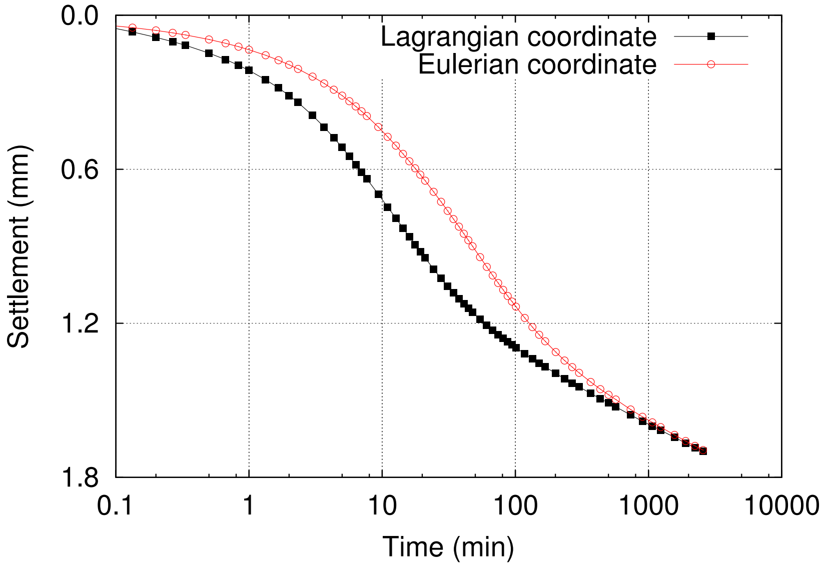

(b) υ_s =70 %

Figure 12: Settlement of the sand-clay mixtures within Eulerian and Lagrangian coordinates (100-200 kPa)

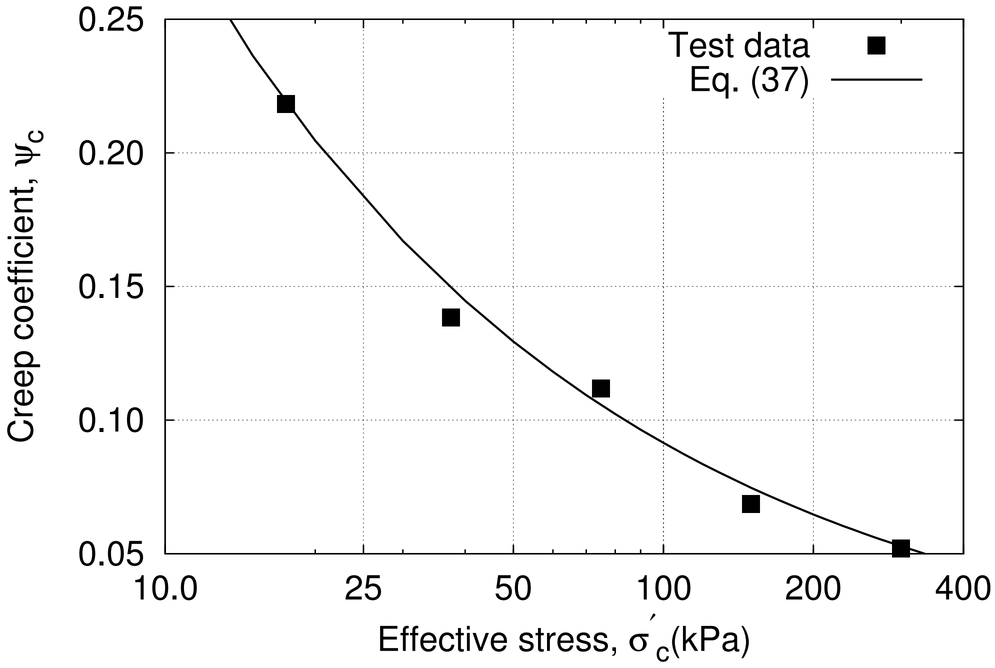

Figure 13: Change of creep coefficient of bentonite matrix

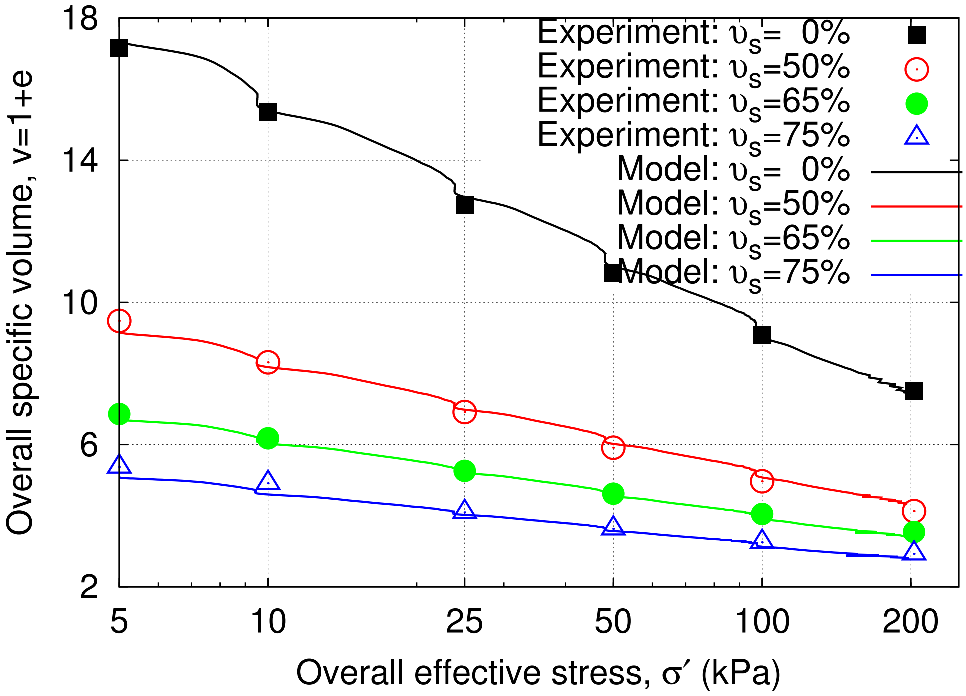

Figure 14: Comparison between the experimental data and the model simulation in v-σ' compression plane (sand-bentonite mixtures)

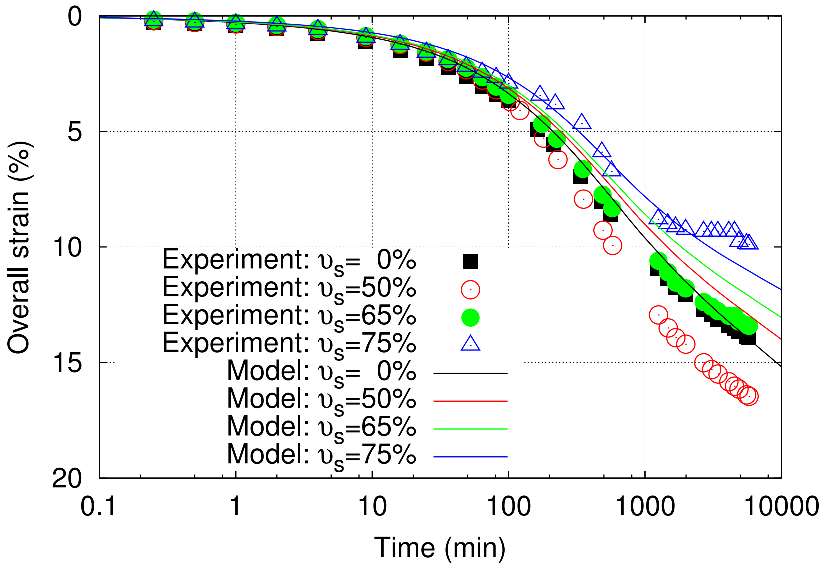

(a) 5-10 kPa

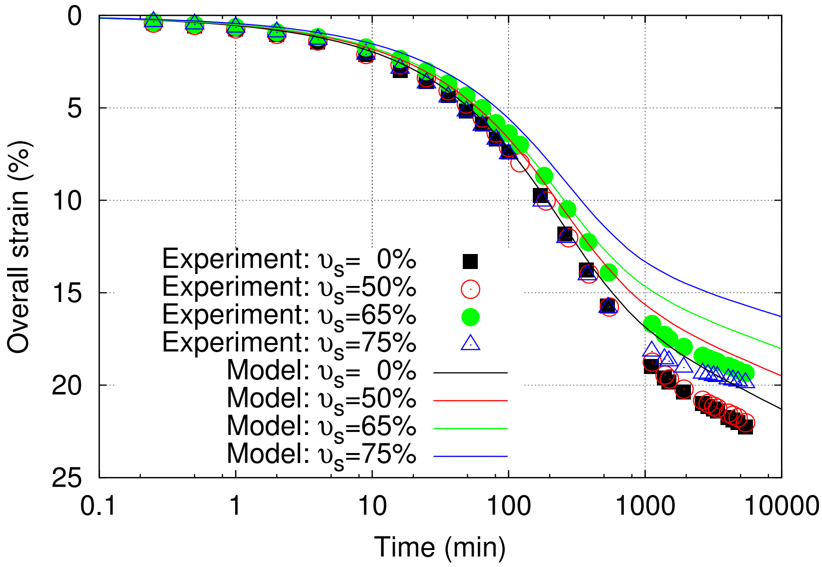

(b) 10-25 kPa

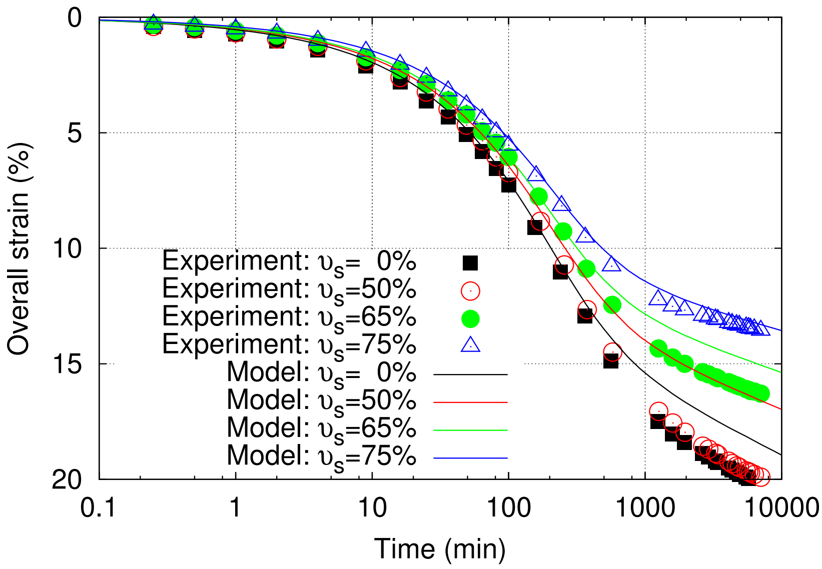

(c) 25-50 kPa

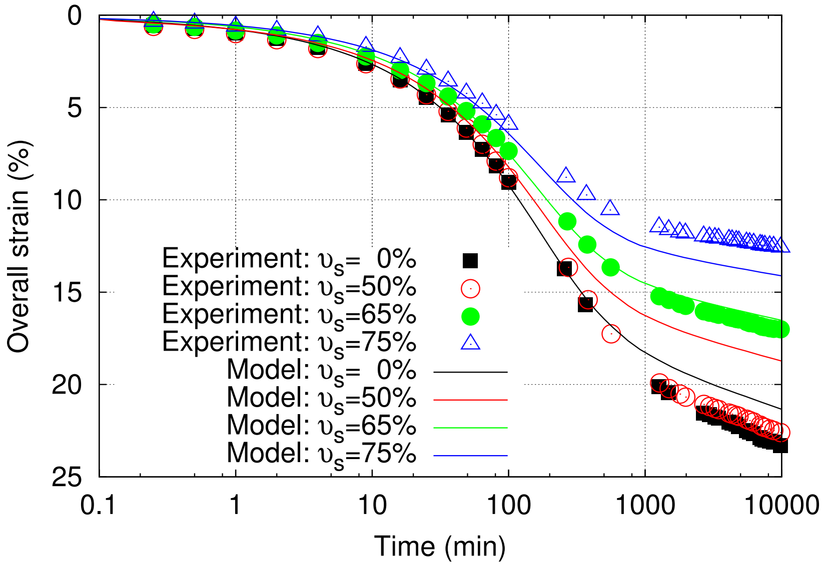

(d) 50-100 kPa

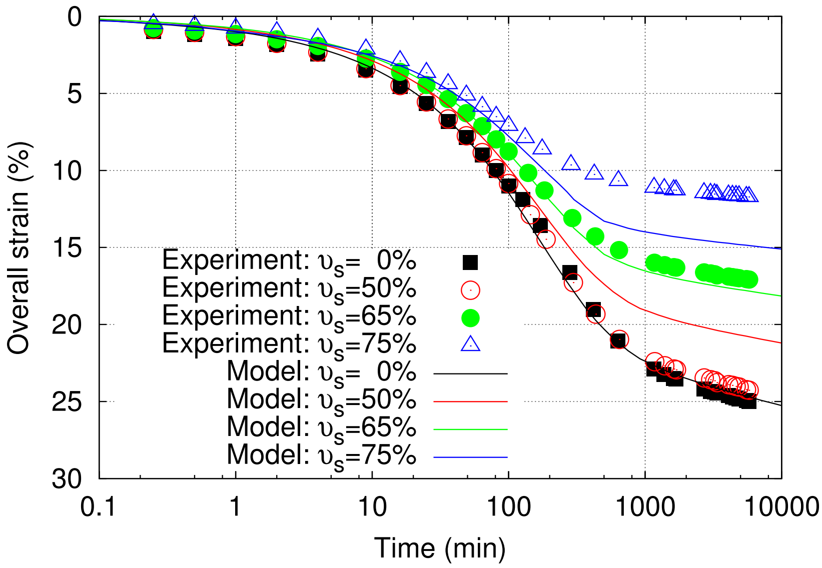

(e) 100-200 kPa

Figure 15: Comparison between the experimental data and the model simulation based on Lagrangian coordinate (Sand-bentonite mixtures)

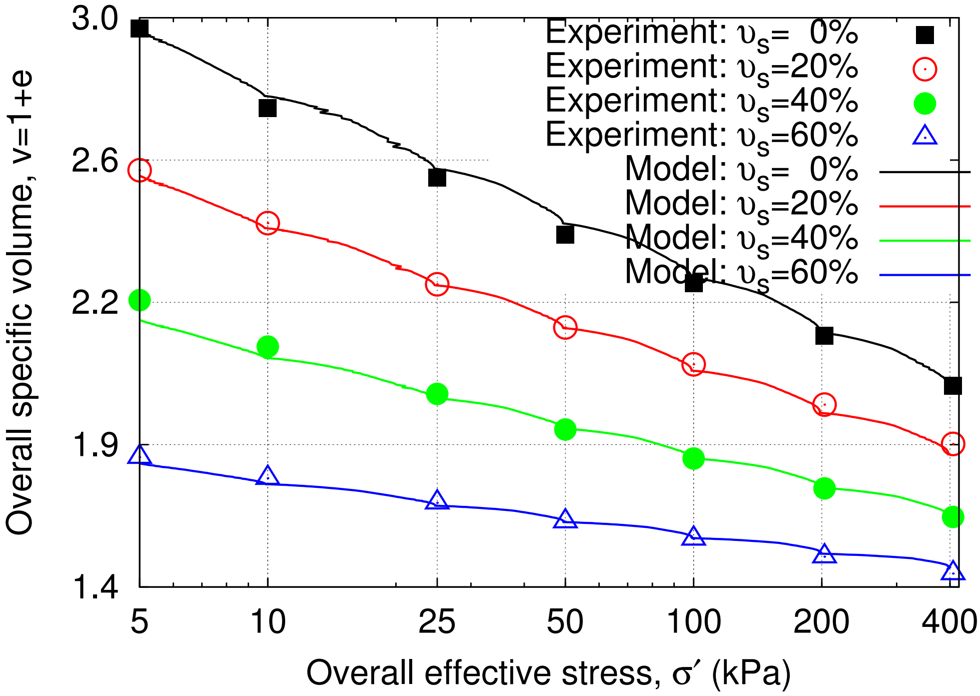

Figure 16: Comparison between the experimental data and the model simulation in v-σ' compression plane (sand-marine clay mixtures)

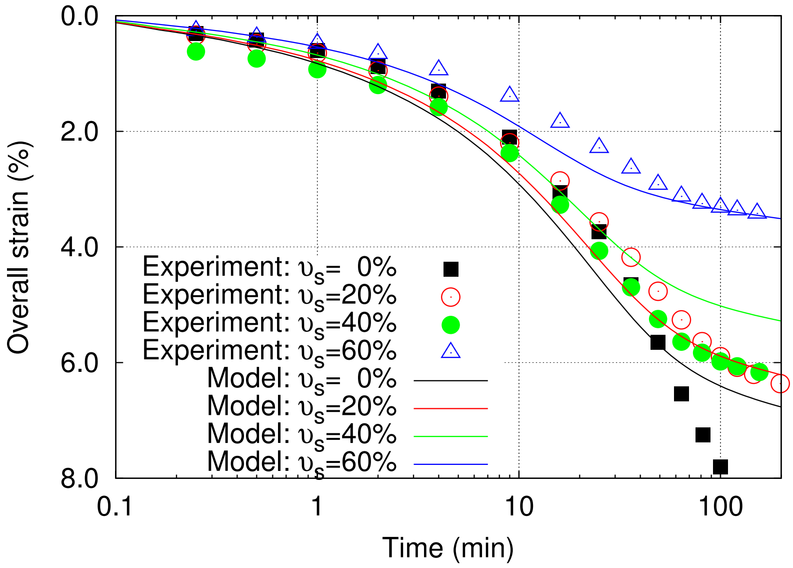

(a) 5-10 kPa

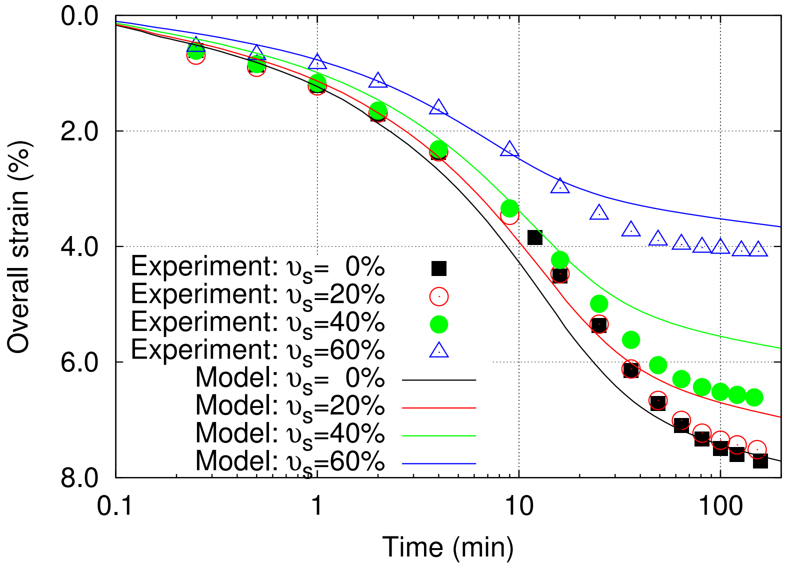

(b) 10-25 kPa

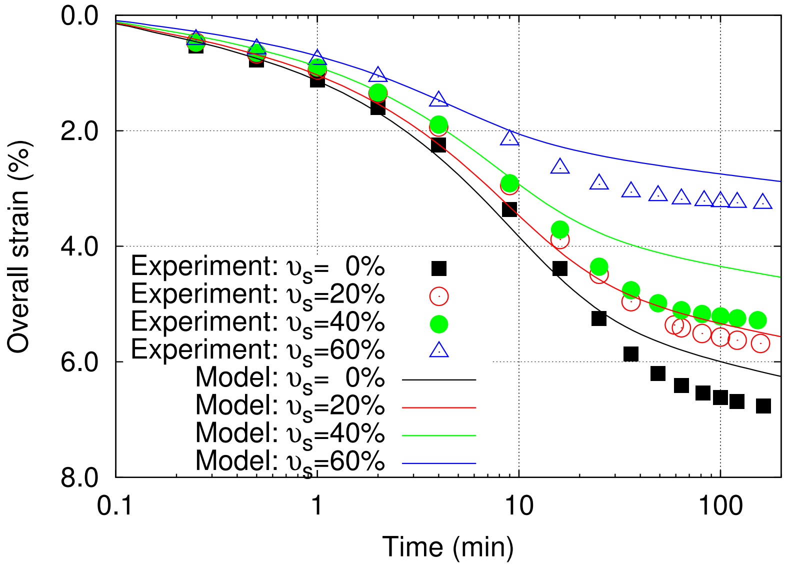

(c) 25-50 kPa

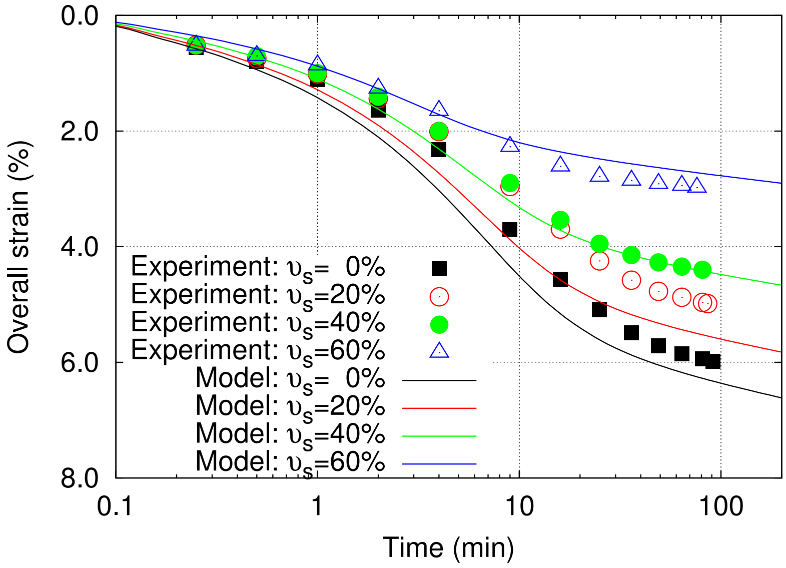

(d) 50-100 kPa

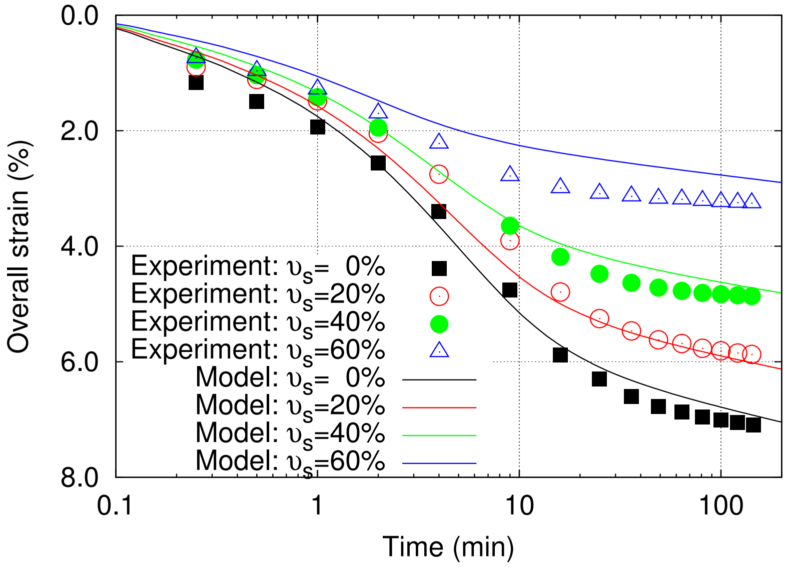

(e) 100-200 kPa

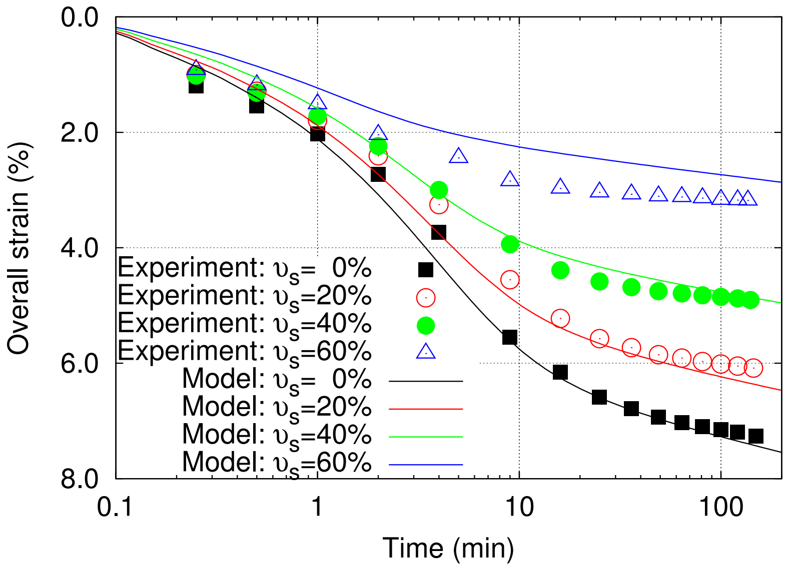

(f) 200-400 kPa

Figure 17: Comparison between the experimental data and the model simulation based on Lagrangian coordinate (Sand-marine clay mixtures)

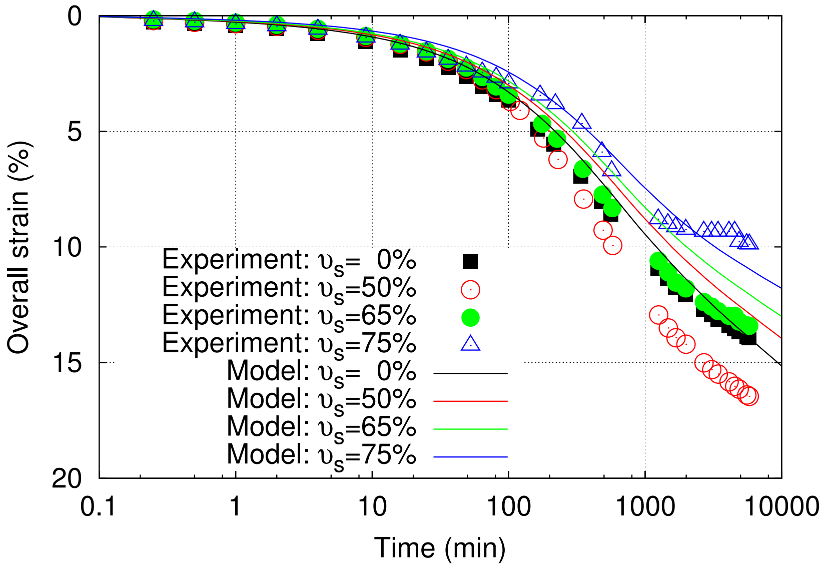

(a) 5-10 kPa

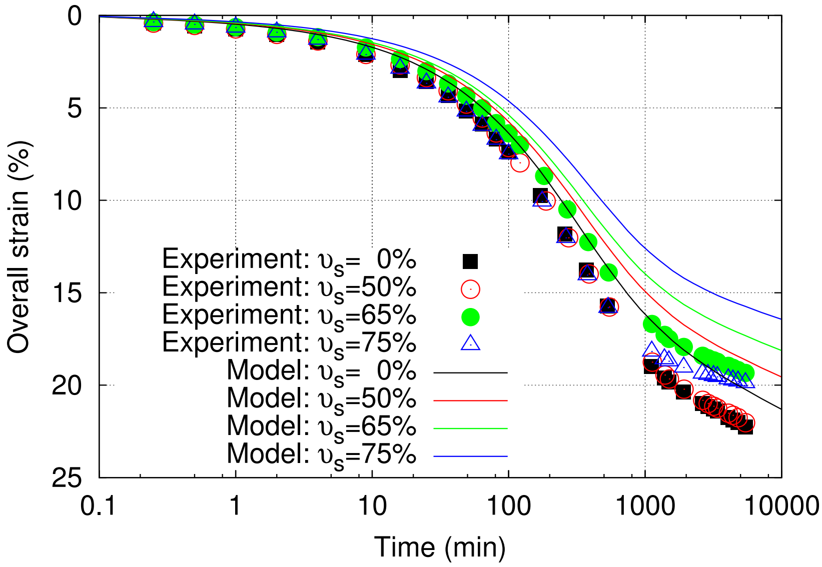

(b) 10-25 kPa

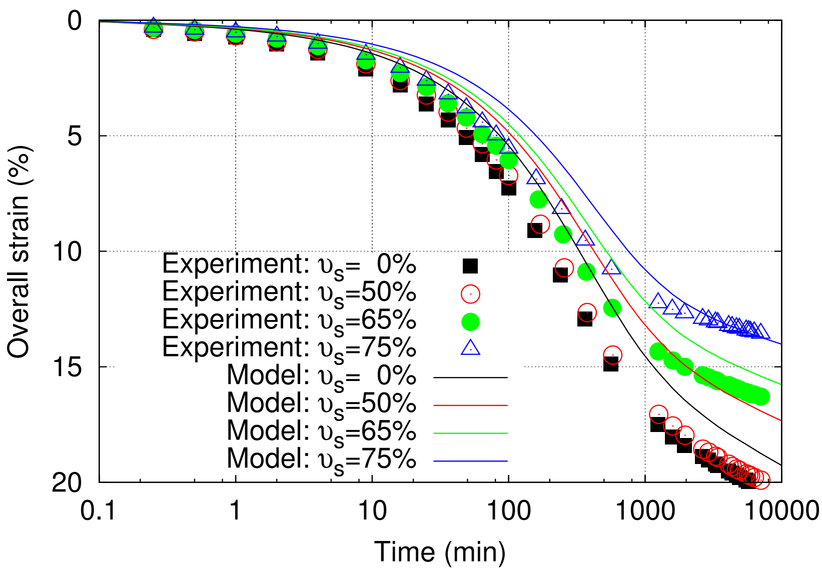

(c) 25-50 kPa

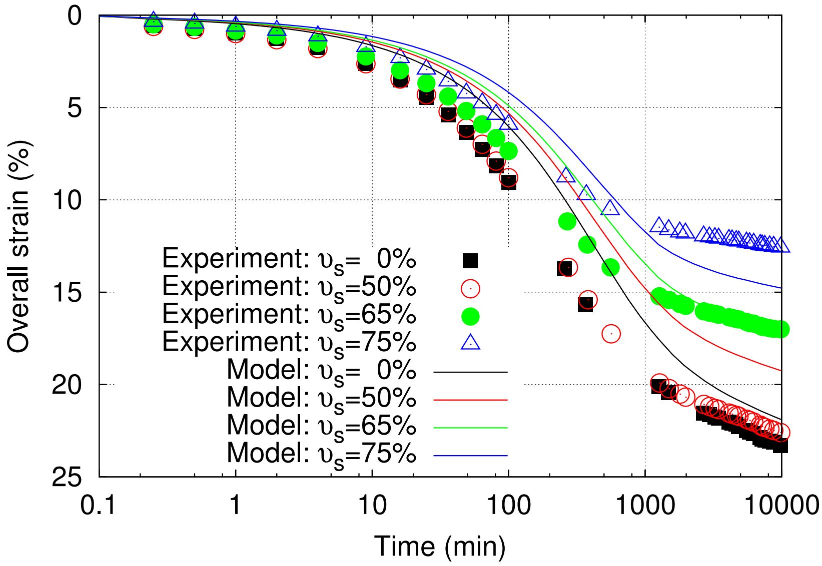

(d) 50-100 kPa

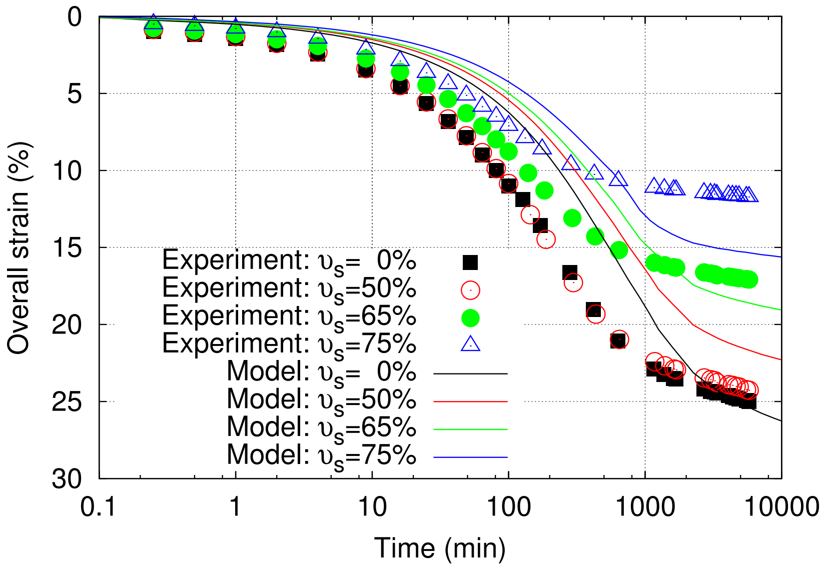

(e) 100-200 kPa

Figure 18: Comparison between the experimental data and the model simulation based on Eulerian coordinate (Sand-bentonite mixtures)